Modification of the GEANT4-DNA source code to enable calculation of the temperature and pH-dependent radiation-chemical yields generated in water radiolysis

Jingyi Bian

Medical Physics Unit
McGill University, Montreal

May, 2023

A thesis submitted to McGill University in partial fulfillment of the requirements of the degree of master of science in medical radiation physics.

Abstract

Radiolysis of water is the decomposition of water molecules into reactive species, including free radicals, positive ions, and molecular products by indirect (x-rays, γ-rays, neutrons) or direct (electrons, protons, heavy ions and other charged particles) energy deposition from ionizing radiation. Given the reactivity of the generated species, water radiolysis studies are of great importance in many domains, such as radiation chemistry and radiation therapy, both in developing detectors such as the hydrated electron detector, the water calorimeter, or understanding the indirect DNA damage. Accurate quantification of the radiation chemical yield (G), defined as the number of chemical entities formed in the radiolysis process by absorption of 100 eV of ionizing radiation, is vital to understand the importance of water radiolysis in these domains. To obtain accurate G-values, the impact of the temperature and the pH need to be considered. Currently, the G-values are obtained from the literature based on experimental studies or calculated by using track structure Monte Carlo software such as the GEANT4-DNA toolkit. To our knowledge, the simulation of water radiolysis with varying temperature and pH using GEANT4-DNA has not been reported. Hence, the main

purpose of this study was to modify the GEANT4-DNA source code to obtain G-values for radiolytic species in the water radiolysis at different temperatures and pH values, perform simulations and compare the results with published work to validate the modifications of GEANT4-DNA package. GEANT4-DNA source code was successfully modified to obtain temperature and pH-dependent G-values for radical species produced in the water radiolysis process. Our temperature-dependent results agreed with experimental data within 0.64% to 9.79% and with simulated data within 3.52% to 12.47%. The pH-dependent results agreed well with experimental data within 0.52% to 3.19% except at pH of 5 (15.99%) and with simulated data within 4.40% to 5.53%. The uncertainties were below ± 0.20%. Overall, our results agreed better with experimental than simulation data.

Abrégé

La radiolyse de l'eau fait référence à la décomposition des molécules d'eau en espèces réactives, telles que des radicaux libres, des ions positifs et des produits moléculaires, par dépôt d'énergie indirecte (rayons x, rayons γ, neutrons) ou directe (électrons, protons, ions lourds et autres particules chargées) provenant de rayonnement ionisant. En raison de la réactivité de ces espèces générées, les études sur la radiolyse de l'eau revêtent une grande importance dans de nombreux domaines tels que la radiochimie et la radiothérapie, à la fois dans le développement de détecteurs tels que le détecteur d'électrons hydratés, le calorimètre à eau, ou dans la compréhension des dommages indirects causés à l'ADN. Une quantification précise du rendement chimique du rayonnement (G), défini comme le nombre d'entités chimiques formées dans le processus de radiolyse par absorption de 100 eV de rayonnement ionisant, est essentielle pour comprendre l'importance de la radiolyse de l'eau dans ces divers domaines. Pour obtenir des valeurs G précises, il est nécessaire de prendre en compte l'impact de la température et du pH. Actuellement, les valeurs G sont obtenues dans la littérature à partir d'études expérimentales, ou sont calculées à l'aide de logiciels de

simulation du passage des particules de la méthode Monte Carlo tel que la boîte à outils GEANT4-DNA. À notre connaissance, aucune simulation de la radiolyse de l'eau prenant en compte les variations de température et de pH à l'aide de GEANT4-DNA n'a été rapportée jusqu'à présent. Par conséquent, l'objectif principal de cette étude était de modifier le code source de GEANT4-DNA afin d'obtenir des valeurs de G pour les espèces radiolytiques présentes lors de la radiolyse de l'eau pour différentes températures et valeurs de pH, de réaliser des simulations et de comparer les résultats avec des travaux publiés pour valider les modifications apportées au code de GEANT4-ADN. Les modifications apportées au code source de GEANT4-DNA ont permis d'obtenir avec succès des valeurs de G dépendantes de la température et du pH pour les espèces radicalaires produites lors du processus de radiolyse de l'eau. Nos résultats dépendants de la température étaient en accord avec les données expérimentales dans une fourchette de 0,64% et 9,79%, et avec les données simulées dans une fourchette de 3,52% et 12,47%. Les résultats dépendants du pH concordaient bien avec les données expérimentales dans une fourchette de 0,52% et 3,19% sauf à un pH de 5 (15,99%), et avec les données simulées dans une fourchette de 4,40% et 5,53%. Les incertitudes étaient inférieures à ± 0,20%. Dans l'ensemble, nos résultats étaient en meilleur accord avec les données expéri-mentales qu'avec les données de simulation.

Acknowledgements

I would like to thank everyone who has made invaluable contributions to my thesis and my master's degree. Firstly, I would like to thank my supervisor Dr. Shirin A. Enger, for her continuous guidance, support, and kindness. Thank you for offering me many opportunities to learn and improve. I would also like to thank my co-supervisor Dr. Hamed Bekerat for helping me do experiments and providing with many useful suggestions. Secondly, I would like to thank all the instructors, professors, staff, and students at McGill Medical Physics Unit for their guidance and help. I want to thank all Enger Lab members for their continuous support and help. I would also like to thank McGill University Health Center and Jewish General Hospital for all the resources. Thank you to the linac engineer at JGH, Mr. Filippo Piccolo, for always helping me figure out the electronic problems. Thank you, Alaina Bui, for guiding me with the lab equipment. Thank you, Julien Mégrourèche, for always helping me figure out the problems I encountered in the measurements. Thank you, Liam Carroll, for helping me with the electronics. Moreover, I want to thank my parents and all my family for their unconditional support.

This research was conducted as part of the activities of MEDTEQ+, thanks to the financial support of the Ministry of Economy and Innovation - PSOv2b program, cofounded by TransMedTech (Canada First Research Excellence Fund), Mitacs, the MUHC Foundation and Varian Medical Systems. Funding from Canada Research Chairs Program (grant # 252135) is acknowledged.

Contents

List of Figures

List of Tables

List of Abbreviations

DNA Deoxyribonucleic Acid

DSB Double-strand Break

ESD Entrance Skin Dose

IRT Independent Reaction Times

LET Linear Energy Transfer

NIST National Institute of Standards and Technology

NPL National Physical Laboratory

PRF Pulse Repetition Frequency

PTB Physikalisch-Technische Bundesanstalt

RNA Ribonucleic Acid

SBS Step-by-step

SSB Single-strand Break

SSD Source-to-surface Distance

UV Ultraviolet

Contribution to Original Knowledge

In this thesis, the source GEANT4-DNA software was successfully modified to enable the calculation of the temperature and the pH-dependent radiation-chemical yields generated in water radiolysis. Although the extensions to the GEANT4-DNA package were done primarily for the development of a hydrated electron detector developed by our group, this work benefits a much larger scientific community. GEANT4-DNA is an open-source platform used by researchers worldwide. In addition to the hydrated electron dosimetry, this work also contributes to water calorimetry as well as to investigations of the indirect action of radical-mediated DNA damage.

Preface and Contribution of Authors

This thesis resulted in one manuscript (Chapter 3): Jingyi Bian, Juan Duran, Wook-Geun Shin, Jose Ramos-Méndez, Jack C. Sankey, Lilian Childress, Jan Seuntjens, Shirin A. Enger. "GEANT4-DNA simulation of temperature-dependent and pH-dependent yields of chemical radiolytic species". This work was presented as an oral presentation at the International Conference on Monte Carlo Techniques for Medical Applications in Antwerp, Belgium. I was invited to submit the manuscript to the focus collection issue in the journal Physics in Medicine and Biology called "Focus on the Monte Carlo Method for Medical Applications: From Macro to Microscale" dedicated to this conference. The manuscript has been accepted in Physics in Medicine and Biology. As the first author, I modified the GEANT4-DNA source code, designed and performed all the simulations and the data analysis required for this manuscript. Juan Duran implemented the original temperature and pH dependency in the GEANT4-DNA code. Wook-Geun Shin and Jose Ramos-Méndez provided help and guidance regarding modifications in GEANT4-DNA. Jack C. Sankey, Lilian Childress, Jan Seuntjens provided general guidance. Dr. Enger

provided guidance throughout the project, reviewed the manuscript continuously and provided feedback on the manuscript.

This work was presented at the following conferences:

1. [Oral Presentation]: Title: Updating GEANT4-DNA to enable simulation of radiation chemical yield of hydrated electrons at different temperatures and pH values.

Author list: Jingyi Bian, Juan Duran, Wook-Geun Shin, Jose Ramos-Méndez, Lilian Childress, Jack C. Sankey, Jan Seuntjens, and Shirin A. Enger.

Conference: International Conference on Monte Carlo Techniques for Medical Applications (MCMA), Antwerp (Belgium), 11-13 April 2022.

2. [ePoster]: Title: Update of the GEANT4-DNA software for simulation of radiation chemical yield for reactive water radiolysis species at different temperature and pH.

Author list: Jingyi Bian, Juan Duran, Wook-Geun Shin, Jose Ramos-Méndez, Lilian Childress, Jack C. Sankey, Jan Seuntjens, and Shirin A. Enger.

Conference: American Association of Physicists in Medicine (AAPM) 2022 64th Annual meeting and exhibition, Washington DC (USA), 10-14 July 2022.

Chapter 1

Introduction

Depending on its ability to ionize matter, radiation can be classified into ionizing and non-ionizing, as illustrated in Figure 1.1. Ionizing radiation refers to neutral and charged particles with sufficient energy to ionize atoms and molecules in the absorbing material they traverse. Ionizing radiation deposits energy in the matter either directly or indirectly. For direct ionization radiation, the charged particles (i.e., electrons, protons, or alpha particles) deposit energy directly through Coulomb interactions with orbital electrons of the atoms in the matter. The indirect ionizing radiation deposits energy in two steps: first, the neutral particles (i.e., photons or neutrons) interact with matter to produce charged particles. Then, the produced charged particles deposit energy to the matter through direct Coulomb interactions. In radiation therapy, charged particles can be categorized into light, intermediate and heavy particles based on their mass (6; 7; 8).

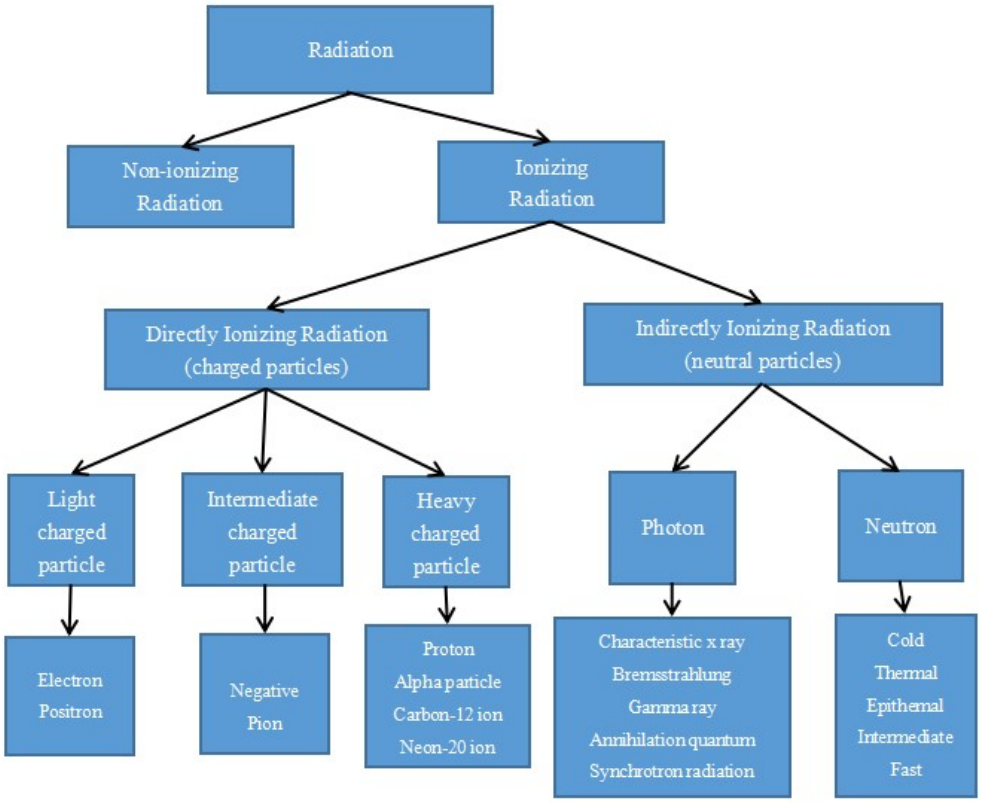

Figure 1.1: The classification of radiation. Figure adapted from (6).

1.1 Radiation Therapy

Cancer is one of the leading causes of death worldwide. Cancer is a disease involving abnormal proliferation of cells through uncontrolled division. In addition, cancer cells can also locally invade surrounding normal tissues and even metastasize to other parts of the body through the circulatory or lymphatic systems in the body (9). The severity of cancer depends on where it is located and the extent of its malignant growth. Treatment of cancer usually includes a combination of chemotherapy, radiation therapy, surgery, and targeted

therapies, including monoclonal antibodies, small molecule inhibitors and targeted radionuclide therapy (10; 11; 12; 13; 14).

Radiation therapy is a local treatment method that uses radiation to treat tumors based on the differences in response to radiation-induced damage between tumor cells and normal cells (15; 16). Radiation therapy aims to kill cancer cells and shrink tumors while causing as minor damage to the surrounding healthy tissue as reasonable. Radiation in radiotherapy includes MV photon, electron, proton, and heavier charged particle beams produced by various therapy accelerators, as well as alpha and beta particles and gamma rays produced by radioisotopes (17; 18; 19).

Ionizing radiation causes DNA damage and sterilizes cancer cells via direct and indirect action of radiation on the DNA molecules. Direct action of radiation refers to the direct interaction of the ionizing radiation with a DNA molecule's atoms, which can cause damage such as DNA single-strand breaks (SSBs), double-strand breaks (DSBs), DNA crosslinks and DNA protein crosslinks (20). It can also indirectly do so by first interacting with other molecules and atoms in the cell, such as water, that subsequently produce short-lived reactive free radicals. Free radicals generated in the DNA molecule surroundings can diffuse and cause damage to the DNA. About two-thirds of the DNA damage by sparsely ionizing radiations (radiation with low linear energy transfer LET (21)) such as x-rays or electrons is due to the indirect action (22; 23; 24; 25; 26). Short-lived species produced in the water radiolysis, such as $^{\bullet}OH$, e^{-}_{aq}, and $H^{\bullet}$, contribute to causing DNA damage (27). The $^{\bullet}OH$ is the most

reactive species to attack, which causes damages to DNA and protein (28; 29). The e^-_{aq} and $H^\bullet$ also contribute to DNA damage by causing base lesions (30).

Absorbed dose, D, is a basic physical quantity that describes the mean energy $\bar{\varepsilon}$ imparted by ionizing radiation to a medium of mass m confined in a finite volume V (6) as described in Equation 1.1.

$$D = \frac{d\bar{\varepsilon}}{dm}. \tag{1.1}$$

1.2 *In vivo* Dosimetry

Radiation dosimetry investigates the quantitative determination of deposited energy in the matter by ionizing radiation (8). The biological effects of ionizing radiation, which primarily refer to the chemical reactions between the short-lived species and cellular components low LET radiation, underscore the significance of dosimetry. Radiation dosimetry is an indispensable basis for applications and research in medical physics, radiation biology, tumor therapy, and radiation protection (20; 22; 31; 32). *In vivo* dosimetry refers to the measurement of the absorbed dose received by the patient during the radiotherapy treatment (33). *In vivo* dose measurements can be used to verify the accuracy of treatment delivery, detect major errors in dose delivery and patient set-up, and record doses received by individual patients. Typical applications of *in vivo* dosimeters are measurements of the entrance skin dose (ESD), which is the absorbed dose received by the

patient's skin during the treatment (34), or transmission dose, which refers to measurements of dose to water behind a patient (35; 36). Advanced *in vivo* dosimeters are needed to measure the dose absorbed by targeted tissue rather than the entrance skin or transmission dose. Currently, no ideal *in vivo* dosimeter exists. The ideal detector material should be water since its radiological properties are similar to human tissues. The current water-based dosimeters are large, which limits the measurement's attainable spatial resolution. Other technologies, such as silicon diodes, can achieve millimeter-scale resolution (37), but they require complex correction factors to convert to tissue-equivalent doses. Both the correction factors and the measurement itself would induce considerable uncertainty. The ideal detector would consist of water, have a small sensitive volume, and be suitable for *in vivo* dosimetry.

Absorbed dose in water can be determined by monitoring the concentration of hydrated electrons, which are short-lived radicals produced by water radiolysis, using fast absorption spectrophotometry (38). The concentration of hydrated electrons in water correlates with the absorbed dose to water. The radiation-induced absorption changes can be measured in water for dose rates delivered in radiotherapy. Still, the optical path required to measure the effect is on the order of meters, making the dosimeter size impractical. Therefore, a design to miniaturize the absorption cell used in a previously developed hydrated electron prototype by our group (39) into a fiber-based Fabry-Perot resonant microcavity is crucial (40). These fiber microcavities incorporate state-of-the-art mirror coatings that can trap the

resonant light for over 100,000 round trips in only a few micrometers, thereby enhancing the light's interaction with the solution. Moreover, the optical fiber interface permits a thin, flexible design suitable for *in vivo* applications. However, one of the main uncertainties in the measurements of the absorbed dose with a hydrated electron dosimeter is the radiation chemical yield (G). This is defined as the number of reactive species' chemical entities, including the hydrated electron formed by the absorption of 100 eV of ionizing radiation in the irradiated solution (41). To obtain precise G-values, the irradiated solution's temperature and pH need to be considered (42; 43). Currently, the G-values are obtained from the literature or calculated using track structure Monte Carlo software packages such as the GEANT4-DNA Monte Carlo simulation toolkit (44; 45; 46; 47). Neither the generic G-values taken from the literature nor those calculated with GEANT4-DNA are based on the specific irradiated solution's pH and temperature. However, at present day, the provided chemical parameters only allow radiolysis simulations at room temperature (25°C) and neutral pH. The simulation of water radiolysis with varying temperatures and pH values using GEANT4-DNA has not been reported. This knowledge and methodology gap inspired the objective of this thesis as we are developing a hydrated electron dosimeter. Calculating the G-value for hydrated electrons generated in the solution used in our dosimeter under correct pH and temperature assumptions is essential for accurate hydrated electron dosimetry.

1.3 Objectives

There are two main purposes in this study. The first purpose was to update the GEANT4-DNA source code by adding temperature- and pH-dependent polynomials/functions of chemical parameters involved in water radiolysis simulation to enable the calculation of G-values for radiolytic species at different temperatures and pH values. The second purpose was to perform simulations with the modified code to obtain temperature- and pH-dependent G-values for radiolytic species, and compare the results with published experimental and simulation work to validate the modifications to the GEANT4-DNA package.

Chapter 2

Literature Review

This chapter focuses on radiation detectors including the hydrated electron detector. Concepts such as water radiolysis, hydrated electrons formed during radiolysis and hydrated electron dosimetry are introduced. Since, the main rationale of this thesis is to modify the GEANT4-DNA package to consider temperature and pH under correct experimental conditions, the current water radiolysis implementation in GEANT4-DNA code is reviewed. Modifying the GEANT4-DNA source coded is needed to accurately determine the hydrated electron G-value for future precise absorbed dose measurement in hydrated electron dosimetry.

2.1 Radiation Detectors

The processes of radiation interaction with matter have been extensively discussed in the literature and will not be further described in this thesis (6; 8). A radiation detector is capable of generating a signal that is directly proportional to the quantity of radiation passing through it. This signal can be used to detect the presence of radiation and determine its precise amount with great accuracy (8). The detector's reading, denoted by M, is a physical property that can be measured and is directly proportional to the dosimetric quantity being measured, denoted by Q. The ratio of the detector's reading to the measured dosimetric quantity (M/Q) is referred to as the detector's response. In order to measure absorbed dose or related quantities of ionizing radiation, a radiation dosimeter is used. However, for use in a clinical setting, a radiation dosimeter must possess numerous desirable properties (48; 49).

1. Reproducible: A detector's reproducibility or precision can be used to assess how well the measured quantity agrees with the expected value under the same conditions or environment. A radiation dosimeter with excellent reproducibility or precision should provide a measured amount that coincides with the expected value within a small uncertainty (8).

2. Linearity: The reading of a radiation dosimeter should be linearly proportional to the measured quantity, such as the absorbed dose. However, linearity usually exhibits only in a specific dose range. Beyond this dose range, the reading tends to saturate (8).

3. High detection efficiency: Detection efficiency is a critical parameter for a radiation dosimeter because it determines how effectively the device can measure the radiation dose. The higher the detection efficiency, the more accurate the dosimeter's measurement will be. The detection efficiency of a dosimeter can be affected by several factors, including the size and shape of the sensitive volume, the type of radiation being measured, and the energy range of the particles being detected. Additionally, the sensitivity of the detector can also affect the detection efficiency, as a more sensitive detector will be able to detect smaller amounts of radiation (8).

4. Directional dependence: Directional dependence of the dosimeter refers to the change in response as a function of the angle of the incident radiation. All dosimeters exhibit specific directional dependence due to structural details and physical dimensions (8).

5. Dose rate dependence: The response of a radiation dosimeter should be independent of the dose rate delivered, at least within a specific dose range. However, in reality, the response of a radiation detector is usually affected by dose rate. Correction factors are needed to account for it (8).

6. Energy dependence: For a radiation dosimeter, the response is a function of energy. An ideal dosimeter system should be energy-independent. However, current dosimeters under the same condition could exhibit linearity at energy E_1, and non-linearity at energy E_2. Correction factors are required to accurately determine

the measured dosimetric quantity (8).

7. High spatial resolution: The spatial resolution of the radiation dosimeter is also an important characteristic. The quantity absorbed dose is a point quantity - the smaller the dosimeter's sensitive volume, the greater the spatial resolution. Ideal measurement requires a point-like detector (8).

8. Simple to use: The dosimeter system should be as simple and convenient as possible, and its implementation must be practically adapted to the clinical setting of radiation. The reusability of the dosimeter system (with a sensitivity almost unchanged) is also an essential factor to consider (8).

Absolute, relative, and reference dosimetry are all important techniques used in acceptance testing, commissioning and quality assurance of radiotherapy equipment to ensure that accurate dose of radiation is delivered to the patients during radiotherapy treatments. Absolute dosimetry is considered the most accurate dosimetry method and is directly measuring the ionization or absorbed dose of radiation under standardized conditions, without relying on a calibration factor. Due to the need for accuracy and consistency in absolute dosimetry, it is typically tied to standard laboratories, responsible for establishing and maintaining a standard such as the National Research Council of Canada Meteorology Research Centre, National Institute of Standards and Technology (NIST) in the United States, the National Physical Laboratory (NPL) in the United

Kingdom, or the Physikalisch-Technische Bundesanstalt (PTB) in Germany. Relative dosimetry involves measuring the response of a dosimeter in a known radiation field, which allows the dosimeter's response to be calibrated to the radiation field. Once calibrated, the dosimeter can then be used to measure the radiation dose or dose rate in an unknown radiation field. Film dosimetry is a form of relative dosimetry. The film is exposed to a known radiation field, and the resulting opacity of the film is related to the absorbed dose. The dose to the film is measured using a reference dosimeter, and the film's response is calibrated accordingly.

Reference dosimeters are used as a standard to define the accuracy of other dosimeters. They are typically calibrated against an absolute dosimeter under standardized conditions to ensure accuracy and reproducibility. Once calibrated, the reference dosimeter can be used to check the accuracy of other dosimeters in use. The use of an absolute dosimeter in the calibration process ensures that the reference dosimeter has a known, traceable accuracy. This is important because it allows for consistency and comparability between different measurements made with different dosimeters. Furthermore, a management protocol is typically established to ensure that the reference dosimeters are periodically checked and re-referenced back to the absolute dosimeter to maintain their accuracy over time. This helps to ensure that the dosimeters remain reliable and accurate for use in radiation measurements. (6; 8).

Radiation detectors can be classified into four major groups: calorimeters, ionization

chambers, chemical detectors and solid-state detectors (8).

Calorimeters (50; 51) determine the energy deposited to a medium by measuring the temperature change caused by the ionizing radiation interaction with the irradiated solution. Due to the relatively direct determination of energy deposition, calorimetry can provide a more accurate absorbed dose. However, these detectors have relatively poor reproducibility and sensitivity mainly due to the thermal resistance of currently available materials (52). Moreover, a correction factor heat defect needs to be used to correct for the radiation-induced chemical changes in water. In graphite calorimeters, a conversion factor is needed to convert the dose in graphite to that in water.

Ionization chambers (6; 8; 53; 54) are detectors that use the ionization effect to measure ionizing radiation. An ionization chamber consists of two electrodes at different potentials and a medium in between. Ionizing radiation produces ionizing ion pairs in the medium. Under the interaction of the electric field, the positive and negative ions drift to the negative electrode and the positive electrode, respectively, to form an ionizing current. The intensity of the ionizing radiation can be obtained by measuring this current since the ionizing current is proportional to the intensity of the radiation. Ionization chambers can be used as a reference dosimeter and an absolute dosimeter and are considered the gold standard for absorbed dose measurements in radiation therapy.

In chemical dosimetry systems (6; 8) the dose is determined by measuring the chemical change produced in the medium (i.e., the sensitive volume of the dosimeter). The energy of

ionizing radiation absorbed in certain media produces a chemical change in the absorbing medium. The amount of this chemical change could be used to measure the absorbed dose. Any well-characterized chemical reaction can be used as the basis for the chemical dosimeter. The most commonly used chemical detector is the Frick dosimeter (55; 56). Fricke dosimeters are based on the oxidation of ferrous ions to iron ions in irradiated ferrous sulfate solutions. The number of ferric ions produced in the solution can be measured by absorption spectroscopy with ultraviolet (UV) light at 304 nm, which is strongly absorbed by ferric ions. Spectrophotometry is used to determine radiation-induced iron ion concentrations. Other commonly used detectors include Alanine (57), Radiographic film (58), Radiochromic film (EBT) (59), Gel dosimeter (60; 61; 62), etc.

Solid-state detectors (6; 8; 63) are radiation detectors with semiconducting materials such as germanium or silicon as the detection medium. These materials are subject to a significant thermal noise level and must be cooled below room temperature. The detection principle is similar to that of the ionization chambers, i.e., when ionizing radiation creates free electrons in the semiconductor, the charge can be collected by applying an external voltage. However, there exists also significant differences between the two detector modalities. In the ionization chambers, the carriers are electrons and positive ions, while for semiconductor detectors the carriers are electrons and holes in the semiconductor material. When a charged particle is injected into a semiconductor, its valence band electrons can absorb the particle's energy and transition to a higher energy band, thus leaving a hole in the valence band (8). Solid-state

detectors are sensitive (3 to 5 eV per ion pair) and suitable for single-event counting with a signal proportional to the energy deposited in the material by the radiation.

2.2 Hydrated Electron Dosimetry

2.2.1 Radiolysis of Water

Radiolysis of water is the decomposition of water molecules (H_2O) by indirect (x-rays, γ-rays, neutrons) or direct (electrons, protons, heavy ions and other charged particles) energy deposition from ionizing radiation with sufficient energy to cause ionization in the traversed medium (64). The phenomenon has been an important area of research in radiochemistry since the 1960s (64; 65). Water radiolysis can be expressed as in the Reaction R1 (65; 66).

$$H_2O \xrightarrow{IR} e^-_{aq},\ H^\bullet,\ {}^\bullet OH,\ H_3O^+,\ H_2O_2,\ H_2,\ H^+ \tag{R1}$$

The radiation-induced decomposition of water can be separated into three stages as illustrated in Figure 2.1: the physical, physico-chemical, and chemical stages, with radiolytic events occurring at specific timescales.

$$H_2O^+ + H_2O \longrightarrow H_3O^+ + {}^\bullet OH \tag{R2}$$

$$H_2O^* \longrightarrow {}^\bullet OH + H^\bullet \tag{R3}$$

$$e^- \longrightarrow e^-_{aq} \tag{R4}$$

The physical stage occurs after the initial interaction with ionizing radiation at 10^{-15} s, where ionized water molecules (H_2O^+), excited water molecules (H_2O^*) and sub-excitation electrons (e^-_{sub}) are formed in spurs, which mean isolated volume elements, along the track of ionizing particles (67). Processes including ion-molecule reaction, dissociative relaxation and thermalization (solvation) of sub-excitation electrons are described in Reactions R2, R3 and R4, respectively. They occur during the physico-chemical stage, from 10^{-15} s to 10^{-12} s. Part of the species in the spurs undergo intraspur reactions in the final stage, called the chemical stage while other species diffuse out in the solution, which occurs from 10^{-12} s to 10^{-6} s (66). By 10^{-6} s, a homogeneous distribution of the species may be assumed.

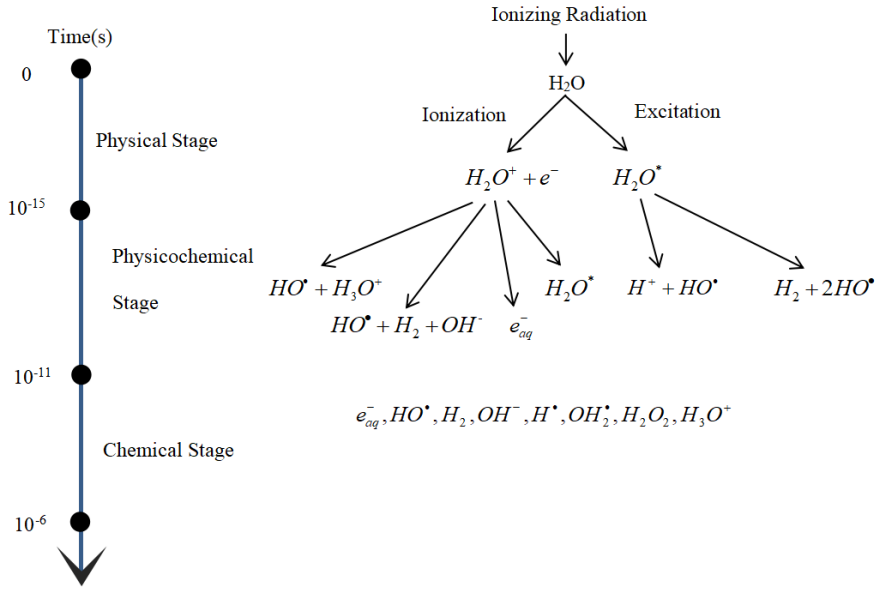

Figure 2.1: Three stages of the water radiolysis process. Figure adapted from (66).

2.2.2 Hydrated Electron

Hydrated electrons (e^-_{aq}) are free electrons ejected from the water molecules during water radiolysis (i.e. physical stage), and were first observed in the early 1960s via pulse radiolysis experiments (38; 68). These electrons interact with the surrounding water molecules, lose their kinetic energy in collisions and thermalize. The electron is then trapped in a potential well that arises from a polarization of the surrounding water molecules via their orientation under the influence of the negative charge (64). This entity, in which the electron is surrounded by several oriented water molecules, forms the so-called hydrated electron (64; 69), as shown in Figure 2.2. The e^-_{aq} is a short-lived and highly reactive species, that reacts with itself, and other species produced in the water radiolysis. Reactions R5 to R9 represent its most important scavenging reactions that occur in pure water. The lifetime of e^-_{aq} in the solution is determined by the occurrence and rate of these reactions.

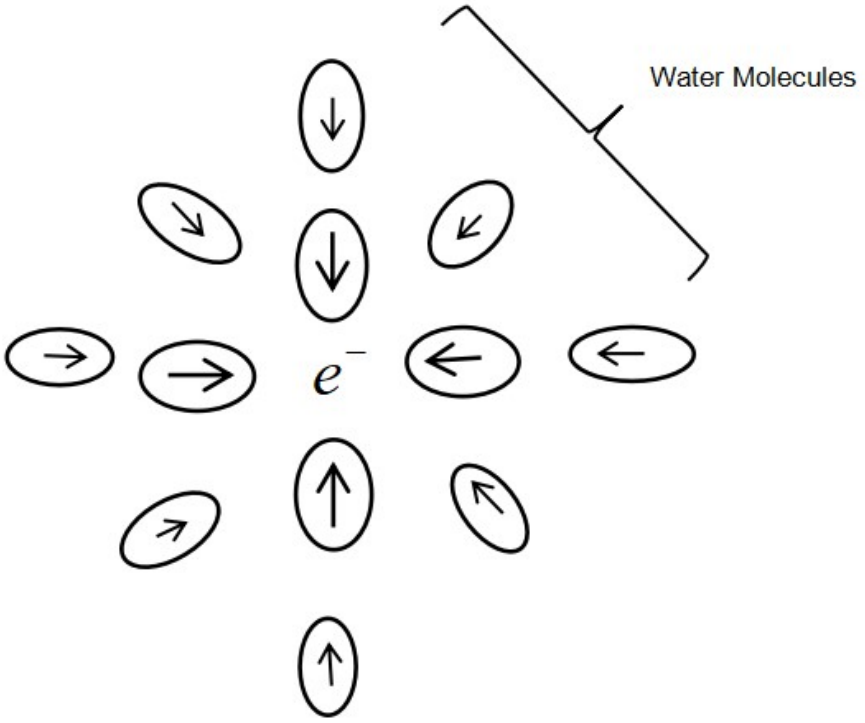

Figure 2.2: Diagram of e^-_{aq}. Figure adapted from (70).

$$e^-_{aq} + e^-_{aq} \xrightarrow{H_2O} H_2 + 2\,OH^- \tag{R5}$$

$$e^-_{aq} + {}^\bullet OH \longrightarrow OH^- \tag{R6}$$

$$e^-_{aq} + H_3O^+ \longrightarrow H^\bullet + H_2O \tag{R7}$$

$$e^-_{aq} + H_2O_2 \longrightarrow {}^\bullet OH + OH^- \tag{R8}$$

$$e^-_{aq} + O_2 \longrightarrow {O_2}^- \tag{R9}$$

$$e^-_{aq} + H^+ \longrightarrow H^\bullet \tag{R10}$$

$${}^\bullet OH + {}^\bullet OH \longrightarrow H_2O_2 \tag{R11}$$

$$H^\bullet + H^\bullet \longrightarrow H_2 \tag{R12}$$

In irradiated water, the e^-_{aq} exhibits an intense optical absorption spectrum, characterized by a broad absorption band with a peak at 715 nm (71).

The pH and the temperature of the solution greatly influence the radiation chemical yield of the e^-_{aq}, $G(e^-_{aq})$, and the G-values for other reactive species. This is because temperature and pH values impact the reaction rate constants of the chemical reactions and diffusion of the species, which are introduced in the embedded manuscript (Chapter 3). The G-value is the number of chemical entities produced per energy deposited by ionizing radiation. G-values are reported in chemical entity per 100 eV (72). The G-values also depend on the LET of the incident radiation, that is the amount of energy transferred to the medium per unit of distance (6). As LET increases, spurs are formed closer in the solution, eventually coalescing into a cylindrical track. As a result, the concentration of radicals (e^-_{aq}, $^{\bullet}OH$, H_3O^+) increases to a point where reactions leading to molecular products (H_2, O_2, H_2O_2) become predominant (73). Therefore, the formation of denser tracks by high LET radiation tends to increase molecular yields but decrease radical yields, notably $G(e^-_{aq})$.

2.2.3 Importance of Water Radiolysis in Dosimetry and Radiation Damage

In calorimetry, a correction factor called the heat defect is needed for accurate absorbed dose measurements. Heat defect corrects for the radiation-induced chemical changes in the water, which causes the temperature rise to be higher or smaller than the value

corresponding to the complete conversion of the energy absorbed by the water into heat. Using the number of primary products produced per energy deposited by ionizing radiation and the subsequent chemical reactions, the chemical changes in irradiated solutions can be simulated using computational models such as the Monte Carlo method, and the heat defects can be calculated (50; 74). In addition, e^-_{aq} dosimetry, which will be discussed in Section 2.2.5, relies on the measurement of the absorbed radiation dose to water by monitoring the concentration of e^-_{aq} using absorption spectrophotometry (71).

Radiation damage is categorized into direct effects caused by ionization or excitation of biomolecules or indirect effects which are chemical modifications induced by reactive oxygen species produced by water radiolysis. In addition to damage caused by reactive species produced in water radiolysis, pulsed radiolysis of water can also be used to elucidate enzymatic reaction mechanisms and to obtain protein structural information in aqueous solutions, such as reduction reactions with protein components, oxidation reactions, redox reactions, protein structure studies, and electron transfer within proteins (75). Water radiolysis has been studied and applied in environmental investigations (76), such as the geological disposal of spent nuclear fuel (fuel oxidation and dissolution) (77). Water radiolysis also contributes to marine sedimentary life. Water radiolysis produces H_2, which can be served as the primary electron donor for microorganisms in continental aquifers several kilometers below the Earth's surface. Therefore, radiolysis products are crucial for sustaining life in seafloor sediments and other planets' subsurface environments (78).

2.2.4 Time-resolved Pulse Radiolysis

Time-resolved pulse radiolysis is an effective method for studying transient species produced in water radiolysis (79; 80). Rapid pulses of high-energy ionizing radiation are used to irradiate water samples encapsulated in quartz cavities. The optical absorbance of the solution is then monitored over time by shining an intense light beam, such as a polychromatic light source (79) or laser pulse (80) through the cavity. The light signal exiting the cavity is focused on a photodetector for readout. The rationale relies on using the optical absorption properties of intermediate species produced in water to obtain information on their nature and reactivity. Parameters such as radical lifetimes and concentrations can be derived from the absorbance measurement. Pulse radiolysis experiments were typically conducted with x-ray and electron beams within the energy range of 1.5 MeV to 30 MeV, delivered by linear accelerators (linacs) with short pulses (10^{-12} s to 10^{-6} s). These pulses were significantly shorter than the lifetime of the intermediate species generated in the solution. The absorbed dose to water typically ranged from 1 Gy to 100 Gy per pulse (64). However, information on dosimetry protocol and irradiation conditions was often missing or incomplete in older radiochemistry reports. This dose range should therefore be interpreted carefully.

2.2.5 Hydrated Electron Dosimetry

Gordon and Hart found that the steady-state concentration of e^-_{aq} could be measured with Co^{60} γ-ray or x-ray sources generating 500 - 1000 rads/sec. In this experiment, a cavity with an optical length of 40 cm was irradiated by a Co^{60} γ-ray source (38; 71). The optical absorption, denoted as $A(t)$, is observed and measured over a period of time, t, using Equation 2.1. The rapid change in transmission intensity from I_0 to $I(t)$ in [mW] was measured and recorded by light from a tungsten filament lamp, which passed through the cavity into a monochromator. The steady-state concentration of e^-_{aq} was calculated with the Equation 2.2 (81). Equation 2.3 establishes a relationship between this concentration and the absorbed dose in water. The absorbed dose ($\bar{D}$) in [Gy] is calculated by Equation 2.4, which involves linearly averaging the absorbed dose over the optical path length of the light source (ℓ) [cm] in the cavity. In this equation, A_{max} represents the maximum absorbance recorded, ρ represents the physical density of the solution in [kg/m^3], and ϵ_λ represents the molar linear extinction coefficient in [$M^{-1} \cdot cm^{-1}$] of e^-_{aq} at the readout wavelength (λ) (73).

$$A(t) = -\log_{10}\left(\frac{I(t)}{I_0}\right) \tag{2.1}$$

$$c_{e^-_{aq}} = \frac{A_{max}}{\epsilon_\lambda \cdot \ell} \tag{2.2}$$

$$D = \frac{c_{e^-_{aq}}}{\rho \cdot G(e^-_{aq})} \tag{2.3}$$

$$\bar{D} = \prod_i f_i \cdot \frac{A_{max}}{\rho \cdot \epsilon_\lambda \cdot \ell \cdot G(e^-_{aq})} \tag{2.4}$$

The highest time resolution of pulsed radiolysis has remained around 30 ps since the late 1960s (82). The 10-90% rise time, considered as the time resolution of the system, is 2 ps. To study the primary processes in the radiation chemistry and physics within 30 ps, a stroboscopic pulse radiolysis system for the absorption spectroscopy with a time resolution of 2 ps was developed by Kozawa *et al.* (2000) (83). The system consists of a sub-picosecond electron linear accelerator as the irradiation source, a femtosecond laser as the analytical light and a jitter compensation system. The time resolution of stroboscopic radiolysis depends on the width of the electron pulse and the width of the laser. Furthermore, the time resolution is limited by the difference between the speed of light and the speed of electron pulses in the sample. In this system, the time resolution is mainly limited by the thickness of the sample (83).

Clinical linacs used in external beam radiotherapy typically deliver ionizing radiation (photon and electron beams) in the form of short pulses, typically lasting 2-5 μs. The pulse repetition frequency (PRF) varies between 180 Hz and 360 Hz, depending on the manufacturer and the chosen beam energy (84). The dose-per-pulse delivered during treatment is on the order of 1 mGy, which is an order of magnitude lower than the minimum absorbed dose previously measured using e^-_{aq} dosimetry (85). The idea of the suitability of the e^-_{aq} dosimetry for low-dose pulses delivered by medical linacs was discussed by Fielden and Hart (1968) (85).

However, the accuracy of Fielden and Hart's measurements was limited by the oscilloscope used at the time. The authors obtained a precision of ±2% down to 1 cGy per pulse of radiation. Beyond this absorbed dose limit the absorbance signal was lost in the noise. This may have been due to the instrumental difficulties with the photodetection system (85).

2.3 Hydrated Electron Dosimetry Prototype

The suitability of e^-_{aq} dosimetry in the very low dose-per-pulse regime (below 1 cGy per pulse) for possible applications in radiotherapy has been investigated in a previous study by Mégrourèche *et al.* (2020) (39). The authors verified the suitability of e^-_{aq} dosimetry in the very low dose-per-pulse regime and the feasibility of employing this technique in radiotherapy (39). Figure 2.3 presents the developed proof-of-concept prototype.

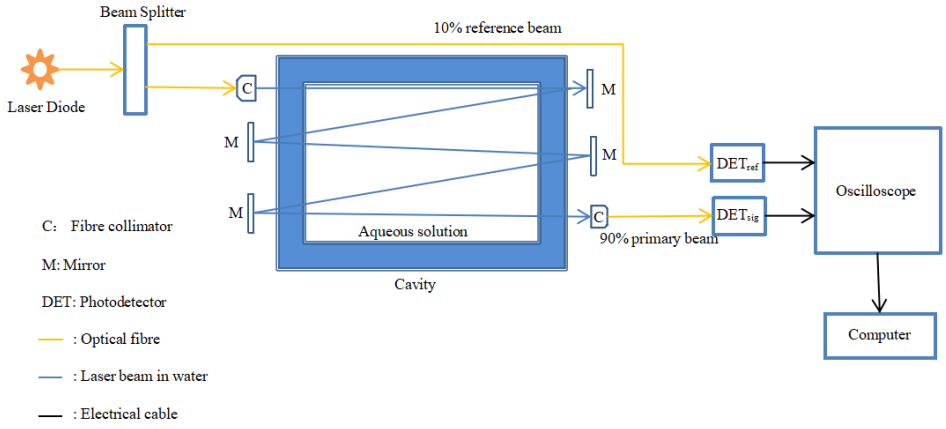

Figure 2.3: Diagram of the e^-_{aq} dosimetry prototype. Figure adapted from (39).

As is shown in Figure 2.3, a probe light source was utilized in the experiment, which

comprised a 45 mW laser diode emitting light at a wavelength of 660 nm. The emitted light was directed onto an absorption cavity with dimensions of $10\times4\times2$ cm^3. The absorption cavity was filled with 60 mL of an aqueous solution. The aqueous solution was prepared by dissolving 0.01 M NaOH in high-purity water. After bubbling with N_2 for thirty minutes, the concentration of dissolved O_2 dropped to ≤ 50 μM. The pH of the solution was determined to be 11.2±0.1. To convert absorbance readings into radiation dose measurements, a $G(e^-_{aq})$ value of 3.0±0.3 [e^-_{aq}/100 eV] was selected from the literature, considering that the absorbance cavity was filled with a basic solution. This conversion was based on Equation 2.4. The laser was sampled into a 10% reference beam and a 90% primary beam. The 10% reference beam was collimated into a separate optical fiber to monitor random fluctuations of the laser diode. The remaining 90% primary beam was reflected back and forth between four broadband dielectric mirrors, as described in (86). Two mirrors were positioned on each side of the cavity, ensuring a total optical path length of 40 cm within the solution. The reflected beam was then collimated and directed back into an optical fiber for readout. Both the reference and primary signals were continuously captured by Si-biased photodetectors with an active area of 0.8 mm^2 and a rise time of 1 ns, as specified in (87). These photodetectors were read out by a 100-MHz bandwidth oscilloscope with a 2-GHz sampling frequency, as specified in (88). The data collected during the experiment was analyzed using an in-house MATLAB program running on a computer. The input and output of the cavity were fiber-coupled, enabling the laser system (diode, temperature, and current controllers) and the

readout system (photodetectors, oscilloscope, computer) to be situated in the linac control room.

The prototype was exposed to photon beams (6 MV, 6 MV FFF, 10 MV FFF) and electron beams (6 MeV) using a Varian TrueBeam™ medical linac. The linac delivers radiation pulses with a duration of 5 μs at a PRF of 180 Hz or 360 Hz, depending on the energy of the beam. Various source-to-surface distances (SSD) were tested to deliver different radiation doses to the prototype, ranging from 0.4 to 2.2 mGy. For the photon beams, an SSD of 70 cm was used, while for the electron beams, an SSD of 98 cm was used. The radiation field size was set to envelop the cavity size (10×4 cm^2), thus covering the entire optical path in the solution. The optical path plane was adjusted to align with the depth of maximal dose (z_{max}) within the cavity. The measured signal comprised oscilloscope recordings with a duration of 500 μs, triggered by the electron gun of the linac so that the absorbance traces precisely coincide the delivery of radiation pulses.

In another study by Bui *et al.* (2021) (89), measurements with EBT3 GafChromic ® films for the same setup and irradiation conditions were performed. The differences between the measured dose from the prototype and the film measurements were within 10% except for the 6 MeV electron beam, where the difference was 15.7%. The large discrepancy for the electron beam can be explained by the larger uncertainty of percentage depth dose for electron beams (89).

2.3.1 Investigation of G(e^-_{aq}) for Improvement of the e^-_{aq} Dosimetry Prototype

According to the Equation 2.4 G(e^-_{aq}) is an important parameter to ensure accurate absorbance measurements (absorbed dose). G-value for e^-_{aq} and other reactive species should be precisely determined. The higher the G(e^-_{aq}), the stronger absorption signal will be detected. G-values depend on the composition of the solution, temperature, pH value, energy of the incoming particle, LET of the incoming beam and many other factors. The composition of the solution should be optimized to remove the species that can react with the e^-_{aq} to slowdown the recombination of e^-_{aq}, and thereby increase the concentration and the lifetime of e^-_{aq}.

Simulation of G-values can be performed by the GEANT4-DNA package (90), which allows us to more accurately determine the G(e^-_{aq}) for a specific setup. However, currently, GEANT4-DNA only calculates G-values for different species at room temperature and a pH value of 7. In this thesis, the GEANT4-DNA source code was modified to calculate G-values for e^-_{aq} and other reactive species at different temperatures and pH values.

2.3.2 Simulation of Water Radiolysis in GEANT4-DNA

Many radiation track structure codes have been developed to simulate the radiation interaction with water and model the formation of radiolytic species, such as PARTRACK (91), RITRACKS (92), TRAX (93), IONLYS-IRT (94) and GEANT4-DNA. The

GEANT4-DNA software is the low-energy extension of the GEANT4 Monte Carlo toolkit (95). It provides a validated simulation platform for microdosimetry and nanodosimetry applications, modeling of DNA damage induced by ionizing radiation, and the water radiolysis process.

Water radiolysis simulations with GEANT4-DNA have been validated with experimental measurements and other simulation packages developed for radiation chemistry applications. Peukert *et al.* (96) showed that the G-values obtained with GEANT4-DNA were consistent with published work. Ramos-Méndez *et al.* (97) observed that $G(e^-_{aq})$ calculated with GEANT4-DNA were in agreement with experimental results (98; 99; 100; 101) within one standard deviation. In water radiolysis simulation with GEANT4-DNA package, the G-values for radiolytic species is calculated using a Monte Carlo simulation which involves event by event tracking the interactions of incident particles with matter and calculating the energy deposited in each voxel of the simulation geometry. The deposited energy is then used to calculate the production of radiolytic species (95; 102). The diffusion and reaction of radiolytic species and their reactive products in water radiolysis simulation with GEANT4-DNA is based on a step-by-step (SBS) method of diffusion-controlled reactions. The diffusion of the chemical species is based on time steps. The time steps can be determined by the user, the time calculated in the simulation, or dynamically (96; 103). The individual molecules of all species of interest are simulated, and the positions of the individual molecules as a function of time are

computed at each time step. At the end of each time step, the probability of chemical reactions for each particle with each neighbor is evaluated by checking the separation distance d of all pairs of reactants. If the distance d is less than the reaction radius R, their products are created, and the old particles are removed. If not, the reactants continue to diffuse. After all the chemical reactions and particle diffusions are finished, the SBS information (i.e., the production of secondary particles, new positions, energy depositions, etc.) is calculated and scored (103; 104; 105; 106). Plante, I. (2011) (107) simulated the water radiolysis with IONLYS-TRACION and IONLYS-TRACELE (108; 109) codes based on the SBS method to calculate the G-values for radiolytic species under different temperatures and pH values. However, IONLYS-TRACION and IONLYS-TRACELE codes are not open-source. In addition, because the SBS method simulates all the particles at every time step, this method requires a huge computation power and time (92; 104). Due to these limitations, many solutions have been proposed to save computational time to simulate water radiolysis more efficiently (110; 111; 112). Among these methods, independent reaction times (IRT) (94; 107; 111; 113; 114; 115; 116) is the most widely used method. The IRT method is based on the independent pairs approximation. In this method, reacting species are described as pairs in all possible combinations. These pairs are considered to be in isolation when reacting. All reaction pairs are stochastically sampled according to the time-dependent survival function suggested by Green *et al.* (1990) (111). Many factors impact the survival function, such as their diffusion coefficients,

reaction radius, Coulomb interaction, the distance between the reacting species, etc. This survival function must be selected according to the type of reaction considered. The pair of reactants having the smallest reaction time is selected as the next reaction that will occur. If products resulted from the reaction, their reaction time with the remaining reacting species is sampled and the corresponding reactions are added to the list of reactions which is resorted. The flowchart of the IRT method can be found in a publication by Ramos *et al.* (2020) (97). This process is repeated until no potential reaction pairs remain or until the cut-off time is reached. The input of the IRT method is the initial spatial distribution of chemical species in the non-homogeneous stage. While the time-dependent spatial information is not explicitly simulated, making the simulation efficient and computationally time-saving.

Goulet *et al.* (1998) (116) compared the SBS and IRT methods. Compared with the SBS method, the IRT method makes the radiolysis simulation more efficient. Despite its limitations such as not calculating the position of reacting species as a function of time, the IRT method is still well suited for water radiolysis simulations.

Another limitation of GEANT4-DNA is its 1 MeV upper limit for electron interaction cross-sections. Bui *et al.* (2021) (117) studied the time evolution of the G-values for the main generated reactive species during water radiolysis using GEANT4-DNA. The effects of cluster size and LET on G-values were examined. The authors found that the time-evolution of the G-value increases with increasing LET for all radiolytic species, and when all factors

are kept constant, as the incoming electron energy increases to clinically relevant energies, $G(e^-_{aq})$ remains similar to its value at 1 MeV. Hence, GEANT4-DNA can be used for clinically relevant energies.

Lastly, the chemical parameters in GEANT4-DNA water radiolysis simulations are only provided at an ambient temperature of 25°C, and neutral pH (97). The simulation of water radiolysis with varying temperatures and pH using GEANT4-DNA has not been reported. Therefore, in this thesis, we implemented the simulation of temperature and pH-dependent G-values for radical species generated from water radiolysis in GEANT4-DNA.

Chapter 3

Body of Thesis

GEANT4-DNA simulation of temperature-dependent and pH-dependent yields of chemical radiolytic species

Objective: GEANT4-DNA can simulate radiation chemical yield (G-value) for radiolytic species such as the hydrated electron (e^-_{aq}) with the Independent Reaction Times (IRT) method, however, only at room temperature and neutral pH. This work aims to modify the GEANT4-DNA source code to enable the calculation of G-values for radiolytic species at different temperatures and pH values.

Approach: In the GEANT4-DNA source code, values of chemical parameters such as reaction rate constant, diffusion coefficient, Onsager radius, and water density were replaced by corresponding temperature-dependent polynomials. The initial concentration

of hydrogen ion (H^+)/hydronium ion (H_3O^+) was scaled for a desired pH using the relationship pH = - $\log_{10}$ $[H^+]$. To validate our modifications, two sets of simulations were performed. A) A water cube with 1.0 km sides and a pH of 7 was irradiated with an isotropic electron source of 1 MeV. The end time was 1 μs. The temperatures varied from 25°C to 150°C. B) Same setup as A) was used, however, the temperature was set to 25°C while the pH varied from 5 to 9. The results were compared with published experimental and simulated work.

Main results: The IRT method in GEANT4-DNA was successfully modified to simulate G-values for radiolytic species at different temperatures and pH values. Our temperature-dependent results agreed with experimental data within 0.64% to 9.79%, and with simulated data within 3.52% to 12.47%. The pH-dependent results agreed well with experimental data within 0.52% to 3.19% except at pH of 5 (15.99%) and with simulated data within 4.40% to 5.53%. The uncertainties were below ± 0.20%. Overall our results agreed better with experimental than simulation data.

Significance: Modifications in GEANT4-DNA code enabled calculation of G-values for radiolytic species at different temperatures and pH values.

Key terms: Radiation chemical yield, Water radiolysis, Radiation chemistry, GEANT4-DNA

3.1 Introduction

3.1.1 Water Radiolysis

When ionizing radiation with sufficient energy interacts with water, it deposits energy along particle tracks, decomposing the water molecules and forming clusters of reactive species known as spurs at each energy deposition point. This process is called water radiolysis (1; 2). Inside the spurs, there exists a competition between the diffusion and reaction of these species as the non-homogeneous concentration gradients relax. Reaction R13 presents a list of the primary and secondary species created in the water radiolysis. The primary species comprise the e^-_{aq}, $^\bullet$OH, H_3O^+, OH^-, H^+ and H_2. While the secondary species encompass the $H^\bullet$, H_2O_2, and H_2. It is noteworthy that H_2 is primarily generated during the initial act of water radiolysis rather than through intraspur reactions, which classifies it as both a primary species and a secondary species (3). Radiolysis of water is divided into three stages: physical stage, physico-chemical stage, and chemical stage (2; 4). The physical stage starts with the initial energy deposition in water leading to the formation of ionized water molecules (H_2O^+), excited water molecules (H_2O^*), and sub-excitation electrons (e^-_{sub}). The physical stage lasts up to 10^{-15} s after the initial interaction with ionizing radiation. The physico-chemical stage follows from 10^{-15} s to 10^{-12} s and consists of processes including ion-molecule reactions, dissociative relaxation, and thermalization (solvation) of sub-excitation electrons (4).

$$H_2O \xrightarrow{IR} e^-_{aq},\ H^\bullet,\ {}^\bullet OH,\ H_3O^+,\ H_2O_2,\ H_2,\ H^+ \tag{R13}$$

The chemical stage is the final stage and takes place from 10^{-12} s to 10^{-6} s. During this stage, the species in the spurs undergo intraspur reactions while others diffuse away from the original point. By 10^{-6} s, a homogeneous distribution of the species is assumed (4; 5). The e^-_{aq} is a highly reactive and short-lived species. The recombination reactions of e^-_{aq} occur in the chemical stage (6). Moreover self-reactions of ${}^\bullet OH$ and $H^\bullet$ also occur in this stage (7). The $H^\bullet$ reacts with water.

3.1.2 Radiation Chemical Yield

The G-value, defined as the number of chemical species created or lost per 100 eV of energy deposited, was introduced in the 1940s by Burton (1947) (8). Obtaining accurate G-values is important in many domains, including the modeling of DNA damage (9; 10; 11) and radiation dosimetry (12; 13; 14; 15; 16). The G-values for different primary species formed in the water radiolysis are dependent on many physical parameters such as the linear energy transfer (LET) of the incoming radiation, temperature, and pH value of the irradiated solution (4; 17; 18).

It is difficult to measure the concentration of the reactive species directly (4). First, under normal experimental conditions, the reactive species' concentration is very low (fractions of a micromole), which requires highly sensitive equipment. The sensitivity of

the experimental equipment can significantly increase the uncertainty of the results. Second, the species' lifetime is short (microsecond), which requires equipment capable of performing rapid measurements. Third, during the measurements, it is necessary to wait until a minimum measurable concentration is reached. The accumulation of products often complicates the observed phenomenon, as the products being accumulated may themselves be susceptible to radiation-chemical changes (e.g. e^-_{aq} can react with itself). Finally, measurement of the G-values for radical species is often based on a product analysis, which involves adding certain solutes before irradiation. To determine the G-values, chemical changes of the solutes are monitored while they react with the species under investigation. However, it is difficult to find solutes that are soluble in water and do not affect its pH (4; 19). Overall, the direct measurement of G-values is challenging. Due to these limitations, simulations with computational models including the Monte Carlo track structure codes were proposed (20). Several studies have used Monte Carlo track structure simulations to investigate different factors such as the energy of the incident radiation (3; 21), cluster size (22) and LET (18) affecting the G-values. Monte Carlo simulations also have been used to investigate dependencies on temperatures and pH values (7; 17; 18; 23).

3.1.3 GEANT4-DNA

Many Monte Carlo track structure codes have been developed to simulate event-by-event radiation interaction in water and the formation of radiolytic species (24; 25; 26; 27; 28; 29)

including the GEANT4-DNA package (30; 31; 32; 33), which extends on the open-source GEANT4 Monte Carlo simulation toolkit (30). However, since GEANT4-DNA is a track structure code, all the ionizations along the charged particle tracks through water are simulated, making the code computationally expensive. In addition to this, the simulation of water radiolysis conventionally is based on a step-by-step (SBS) approach adding to the computational cost both in power and time (24; 30; 34; 35; 36). To alleviate this, variance reduction techniques (37) and a combination of condensed-history and track-structure transport (38) were implemented during the physical stage while the independent reaction times (IRT) technique was implemented for simulating the reaction kinetics of chemical species during the chemical stage (39).

The IRT method is well suited for water radiolysis simulations due to its efficiency compared with the SBS method. As of today, the simulation of water radiolysis with varying temperatures and pH values using GEANT4-DNA has not been reported. Simulation of water radiolysis with varying temperatures and pH values, and studying the influence of these parameters on the G-values for the generated radical species need to be further investigated.

3.2 Aim

The aim of this study was to further develop the GEANT4-DNA source code to allow users to obtain G-values for reactive species produced in water radiolysis at different temperatures

and pH values. This study also aims to perform simulations of G-values for these species to validate the modifications in the code.

3.3 Materials and Methods

In the following section, a brief summary of the implementation of the IRT method in GEANT4-DNA is given, which is necessary to understand the changes made in the code for obtaining the G-values for reactive species at different temperatures and pH values.

3.3.1 Chemical Parameters in Water Radiolysis Simulation

Chemical parameters that have an impact on the simulation process of water radiolysis in the IRT method are reaction rate constant, diffusion coefficient, the Onsager radius (r_c), and water density (34; 35; 40; 41; 42; 43). Reaction rate constants are used to quantify the rate and direction of the water radiolysis reactions and have a great impact on the water radiolysis process. The diffusion coefficients are used to describe the diffusional motion of molecules in solution or the kinetics of reactions between reactants. The smoluchowski diffusion equation and the Debye-Smoluchowski equation have been widely used to simulate this transportation. A detailed derivation of the theory of diffusion is presented in published work (36; 44; 45; 46).

The reaction radius, R, which refers to the threshold at which the reactants can react is calculated by the Smoluchowski diffusion equation:

$$R = \frac{k}{4\pi N_{\mathrm{A}} D}, \tag{3.1}$$

where N_A is Avogadro's number, k is the effective reaction rate constant (including re-dissociation), and D is the sum of the diffusion coefficients of molecules. The radical species are diffused based on their temperature-dependent coefficients. In general, an electron is simulated down to the energy limit of the physical models, then it is stopped and moved a distance randomly sampled from an energy-dependent thermalization curve (47; 48). Hervé du Penhoat *et al.* (2000) (7) studied the effect of temperature on this thermalization distance and found that the electron thermalization distance decreases with increasing temperature. The Onsager radius represents the range of the Coulomb interaction in a particular system. It is defined as the distance at which the electrostatic energy of a pair of elementary charges (electrical charge e_A and e_B) falls to the thermal level. The probability of reaction for diffusion-controlled reactions between charged particles is affected by the Onsager radius (34; 45; 49). The temperature-dependent Onsager radius is defined by the Equation 3.2:

$$r_c = \frac{e_A e_B}{4\pi\varepsilon k_B T}, \tag{3.2}$$

where k_{B} is Boltzmann's constant, ε is the relative permittivity of the solvent (water), and T is the absolute temperature of the medium in Kelvin (for water, $r_c \approx 0.715$ nm at 25°C) from (36).

The IRT method takes information from a particle's position at the end of the

pre-chemical stage, as well as parameters such as the reaction rate constants and diffusion coefficients, to calculate the reaction time of a given reaction (46; 50). The water radiolysis simulations with the GEANT4-DNA using the IRT method result in a large number of reactions, e.g., 15 species and 72 reactions for the time beyond the microsecond range that includes both heterogeneous and homogeneous chemistry stages (51; 52). For the time range below 1 μs, previous studies demonstrate that between 10 to 14 reactions are sufficient to obtain accurate G-values compared to measured data (7; 53). The reaction rate constants are presented in Table A1, A2, A3, A4, A5, A6, A7, A8 in Appendix A, and the diffusion coefficients are presented in Table B1 and B2 in Appendix B. As presented in the Appendices, chemical parameters, such as reaction rate constant and diffusion coefficient, can be described as functions of temperature. These parameters were made temperature-dependent in this study, by taking values from the literature (54; 55; 56; 57; 58).

The density of water also changes with temperature along the liquid-vapor coexistence curve (59), as shown in Equation 3.3. That is, there exist pressure-temperature combinations at which the two phases can coexist, as described by the liquid-vapor coexistence curve (60; 61).

$$\rho(g/mL) = 0.999 + 1.094 \times 10^{-4}t - 7.397 \times 10^{-6}t^2 + 2.693 \times 10^{-8}t^{-3} - 4.714 \times 10^{-11}t^4 \quad (3.3)$$

3.3.2 Simulation Setup

In this project, additional flexibility was added to GEANT4-DNA to configure the input chemical parameters of the IRT method. The GEANT4-DNA package version 10.07 was used. The values of the chemical parameters mentioned above (reaction rate constant, diffusion coefficient, the Onsager radius, and water density) at ambient temperature (25°C) were replaced with corresponding temperature-dependent polynomials. Reaction rate constants presented in Table A1, A2, A3, A4, A5, A6, A7, A8 in Appendix A, were made temperature-dependent by taking the values from (54; 55; 56). Diffusion coefficients presented in Table B1, B2 were made temperature-dependent by taking the values from published work (54; 57; 58). The temperature-dependent Onsager radius described in Equation 3.2 decreases as the temperature increases from 25°C to 150°C. As shown in Equation 3.3, all simulations were performed with the liquid-vapor coexistence curve. As the temperature increases from 25°C to 150°C, the density of pressurized water varies from 1 g/mL (0.003 MPa) to 0.917 g/mL (0.477 MPa) (62).

Regarding the pH dependence, pH generally represents the concentration of H_3O^+ and OH^-, which affects the type 6 reaction rates as described in Section A and presented in Table A8. Since one of the reactants in type 6 reactions has a considerably bigger concentration than other reactants and is considered a background molecule, the reaction rate is the product of the observed reaction rate of the reaction and the concentration of the background reactant. The product is called the scavenger capacity and is considered to

be the reaction rate of the reaction (63). Background molecules in this model are the H_3O^+, the OH^-, and water (H_2O). The concentration of OH^- and H_3O^+ varies depending on the input pH.

In addition, several changes were made to the chemistry modules of the GEANT4-DNA source code. Two new methods for enabling change of the temperature and the pH by the users were added to the G4DNAChemistryManager class (64). This class is called from the physics models and is responsible for creating the water molecules and the solvated electrons and sending them to the G4ITStepManager class to be treated in the chemistry stage. A new constructor that takes temperature and pH as input was added to the G4EmDNAChemistry_option3 class (65; 66), which defines molecules, chemical reactions, and dissociation schemes (67). All molecules' temperature-dependent diffusion coefficient values (as presented in Table B1, B2) were instantiated in this class. A new method called ConstructReactionTablePhTemp was implemented to initialize the reaction rate constants of all the reactions with temperature-dependent polynomials (presented in Table A1, A2, A3, A4, A5, A6, A7, A8), and the concentrations of OH^- and H_3O^+, which vary depending on the input pH. In addition, the G4DNAMolecularReactionTable class, which contains a table of chemical reactions and parameters (67), was modified so that the users can set and get the temperature for the solution. The Onsager radius with temperature-dependent polynomial was initialized in this class. Apart from the scaling of temperature and pH-dependent values, all algorithms, chemical and physical models remained unchanged.

G4EmDNAPhysics_option2 (32; 68) physics constructor was used in this work.

To enable GEANT4-DNA users to benefit from the added features, a GEANT4-DNA example user code called chem6 was modified (35). After the modifications, the user code was called Chem_Temp_pH. Water density with temperature-dependent polynomial was initialized in the DetectorConstruction class of Chem_Temp_pH. In addition, a constructor that takes the temperature and pH of the solution as input was added to its PhysicsList class.

3.3.3 Validation of the Modification

Two sets of simulations were performed to validate our additions to the GEANT4-DNA source code. In the first set of simulations, G-values' dependency on temperature (from 25°C to 150°C) for radiolytic species was examined. A semi-infinite water cube (mimic as 1 km sides) was irradiated with an isotropic point source of 1 MeV electrons placed in the center of the phantom. The rationale for using 1 MeV electrons was based on the upper limit for electron interaction cross-sections in GEANT4-DNA, and to simulate a setup that was closer to published pH and temperature studies, such that we could compare our results with these published studies. Experiments performed by Elliot *et al.* (1993) (69) are conducted with 2.25 MeV electrons. However, as described above, GEANT4-DNA has an upper energy limit of 1 MeV for electron interactions. Nevertheless, Pimblott and LaVerne (1998) (70) demonstrate that above 100 keV, the G-values produced by electrons are unaffected by

the electron's initial kinetic energy. The 1 km side water cube was chosen to mimic an infinite volume to ensure that all the secondary particles and reactive species do not leave the volume (3). Primary electrons with the incoming kinetic energy of 1 MeV were killed if deposited energy was greater than 10 keV by the Primary Killer class, thus ensuring a constant ionization density (70; 71). The end time for the simulation was set to 1 μs due to the homogeneous distribution of the radical and molecular products, which is assumed by about 1 μs after the ionizing event (end of the chemical stage). The water pH was set to 7. The simulations were performed at 25°C, 50°C, 75°C, 100°C, 125°C and 150°C. The second set of simulations examined the dependency of G-values on pH. The same phantom and source characteristics were used. However, the temperature was kept constant at a value of 25°C, and the simulations were performed at pH values of 5, 6, 7, 8, and 9. Ten runs were performed, with each run consisting of 1000 incoming electrons. Each run took minutes.

In this work, data was collected from 10^{-3} μs to 1000 μs. Totally 50 data points were collected in this time range. G-values at 1 μs were collected and compared with published experimental and simulation data. Percentage differences between the results in this work and published data were calculated to verify our implementation of the GEANT4-DNA package. Another way of verifying our implementation was to perform the *material balance test*, which assumes balance between the reducing species and oxidizing species produced in the water radiolysis process (4; 7; 72). The material balance test verifies if the chemical system conserves material by computing the equilibrium states which evolve from initial

states by the processes of chemical reaction and diffusion (73). The material balance can be expressed as the equation below:

$$G_{red} = G_{ox} \tag{3.4}$$

$$G_{red} = G(e^-_{aq}) + 2G(H_2) + G(H^\bullet) \tag{3.5}$$

$$G_{ox} = G(^\bullet OH) + 2G(H_2O_2) + 3G(HO_2) \tag{3.6}$$

3.4 Results and Discussion

3.4.1 Effect of Temperature on G-values for Reactive Species

Figure 3.1 shows the G(e^-_{aq}) at different temperatures from 25°C to 150°C simulated in this work. The results were compared with the published experimental data (56; 74) and simulation results from Monte Carto track structure codes IONLYS-TRACION and IONLYS-TRACELE (18) and from TRACIRT (7). The G(e^-_{aq}) at all temperature points shown were: 2.59 (25°C), 2.69 (50°C), 2.75 (75°C), 2.80 (100°C), 2.89 (125°C) and 3.03 (150°C). The uncertainties were averaged across all simulated particles and then propagated across all executed runs. In this work, the uncertainties of the temperature-dependent G(e^-_{aq}) were less than 0.18%. Our results agreed with the experimental data within 0.64% ± 0.18% to 9.79% ± 0.16% (56; 74). Considering the

difficulties of temperature and pressure control in the experimental setup and measurement errors in determining the radiolytic yields, the results are acceptable. Regarding simulation results performed with other code packages, our results agreed with the data within 3.52% ± 0.17% to 12.47% ± 0.15% (7; 18). As can be seen in Figure 3.1, overall our results agreed better with published experimental work than with simulation results performed with other code packages. With increasing temperature, the $G(e^-_{aq})$ undergoes a gradual increase primarily due to two processes: self-recombination of e^-_{aq} and its reactions with other primary or secondary species. The recombination of e^-_{aq} ($e^-_{aq} + e^-_{aq} \rightarrow H_2 + 2OH^-$) and its reaction with H^+ ($e^-_{aq} + H^+ \rightarrow H^\bullet$) are both controlled by diffusion, while its reaction with $^\bullet OH$ ($e^-_{aq} + {}^\bullet OH \rightarrow OH^-$) is partially influenced by diffusion. Although the diffusion of species increases with temperature, the reaction rate constant of the reaction between e^-_{aq} and $^\bullet OH$ does not increase proportionally. As the temperature rises, a greater number of e^-_{aq} become available for either diffusing out of the spur or participating in the spur's reactions through self-recombination and reaction with $H^\bullet$ to form various molecular products, predominantly H_2. Overall, both $G(e^-_{aq})$ and $G(H_2)$ demonstrate an upward trend with increasing temperature. (7; 75; 76).

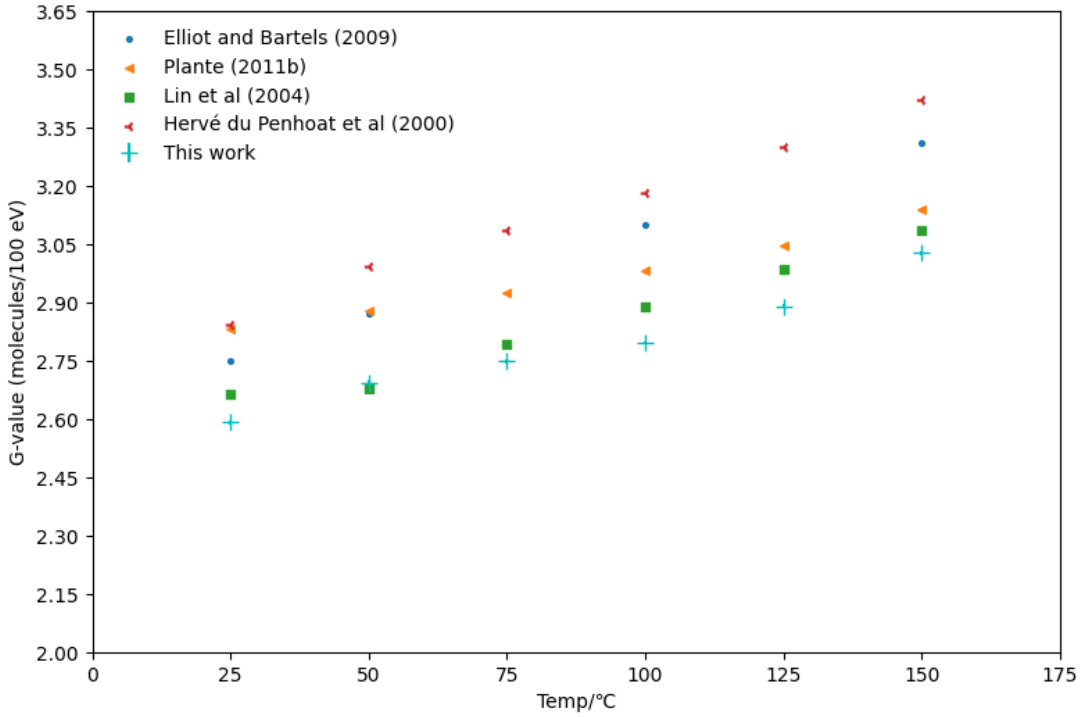

Figure 3.1: G(e^-_{aq}) at the temperature range from 25°C to 150°C simulated in this work and comparison with the published work. The results were compared with the published experimental data (56; 74), and simulation results from Monte Carto track structure codes IONLYS-TRACION and IONLYS-TRACELE (18) and from TRACIRT (7).

In addition to the e^-_{aq}, the G-values of oxidizing species, namely the $^{\bullet}$OH and H_2O_2 were computed and assessed. The results are presented in Figure 3.2. G($^{\bullet}$OH) and G(H_2O_2) were simulated at various temperatures ranging from 25°C to 150°C. These values were then compared with published experimental data (56), as well as simulation results obtained from Monte Carlo track structure codes IONLYS-TRACION and IONLYS-TRACELE (18),

and TRACIRT (7). The trends observed in the G($^{\bullet}$OH) and G(H_2O_2) values align closely with the trends reported in the published data. As the temperature increases, G(H_2O_2) decreases, which is consistent with the findings reported by Plante (2011) (18). This behavior can be attributed to the fact that H_2O_2 is predominantly formed through the self-reaction of $^{\bullet}$OH. The temperature-dependent G(H_2O_2) simulated in this study agrees with the outcomes presented by Hervé du Penhoat *et al.* (2000) (7). The authors concluded that the reaction rate constant for the self-reaction of $^{\bullet}$OH decreases with temperature, leading to an increase in G($^{\bullet}$OH) and a decrease in G(H_2O_2) (7).

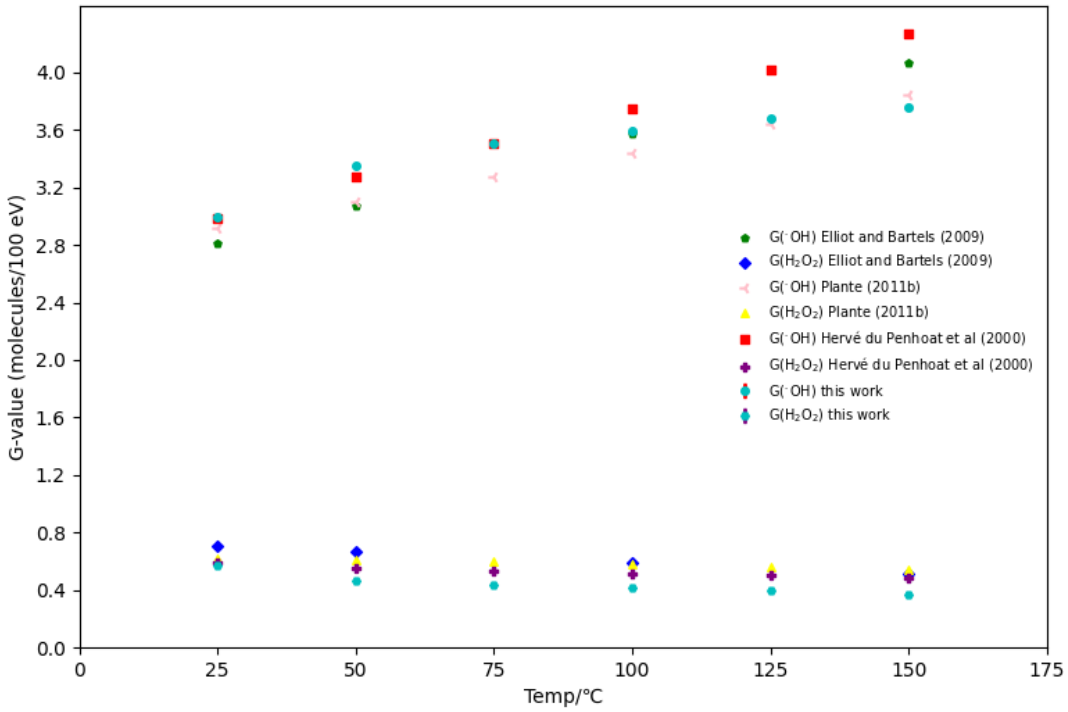

Figure 3.2: G($^{\bullet}$OH) and G(H_2O_2) were simulated in this study within the temperature range of 25°C to 150°C. These simulated values were then compared to published experimental data (56), as well as simulation results obtained from Monte Carlo track structure codes IONLYS-TRACION and IONLYS-TRACELE (18), and TRACIRT(7).

Figure 3.3 illustrates the time-evolution of G-values for reactive species generated at different temperatures ranging from 25°C to 150°C, considering an incoming electron energy of 1 MeV. The time interval was limited to 1 μs, as described in Section 3.3.3. The uncertainties associated with G($H^{\bullet}$), G(H_2), G(H_2O_2), G($^{\bullet}$OH), and G(OH^-) at various temperatures were found to be within 0.31%. In general, as observed in the simulation by

Plante (2011) (18), the G($^{\bullet}$OH) and G(H$^{\bullet}$) decreased over time due to radical recombination, leading to the formation of molecular products. Conversely, the G(H_2) and G(H_2O_2) increased as a function of time. As demonstrated in Figure 3.3, the G(H_2) exhibited an increase with temperature. This can be attributed to the fact that H_2 is primarily generated through the recombination of the e^-_{aq} ($e^-_{aq} + e^-_{aq} \rightarrow H_2 + 2OH^-$), which is a diffusion-controlled reaction. Consequently, the reaction rate constant for this process increases at a greater rate than the rate at which individual species diffuse out of the spur. As temperature rises, the recombination of radical species within the spurs occurs at a faster rate compared to diffusion, resulting in the production of a greater number of molecular recombination products (7). On the other hand, the G(H$^{\bullet}$) value did not significantly change as the temperature increased. This can be attributed to four different reactions involved in the generation and decay of H$^{\bullet}$, which include the interactions of e^-_{aq} and H^+ leading to H$^{\bullet}$ formation, H$^{\bullet}$ reacting with $^{\bullet}$OH to produce H_2O, e^-_{aq} reacting with H$^{\bullet}$ resulting in H_2 and OH^-, and finally, e^-_{aq} reacting with H_2O leading to the formation of H$^{\bullet}$ and OH^- (7).

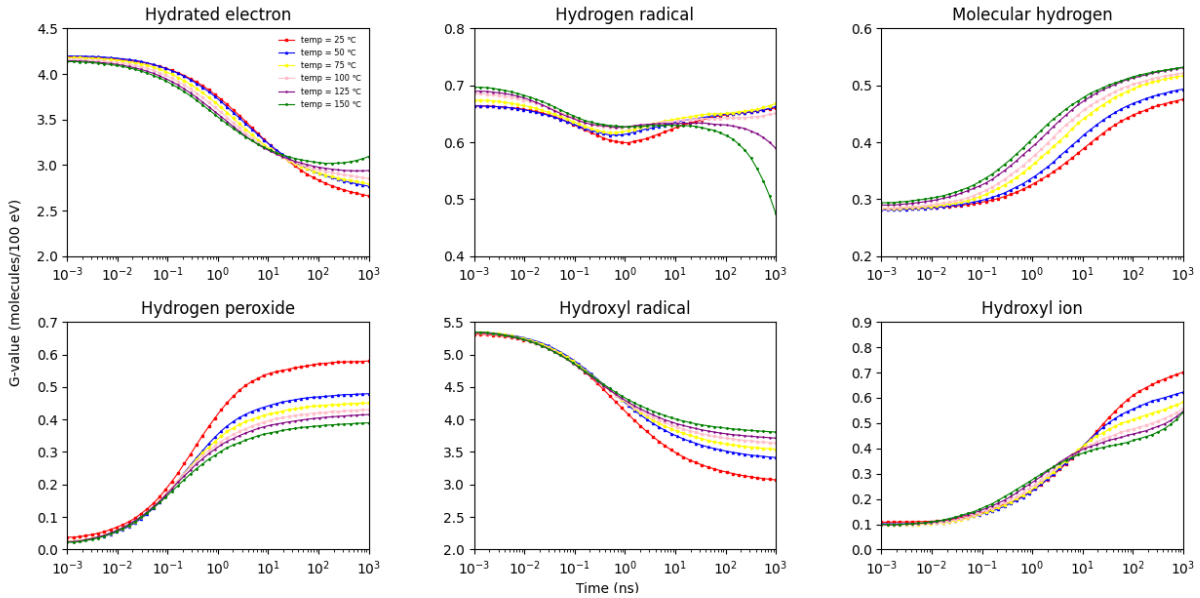

Figure 3.3: Time-evolution of G-values for generated reactive species at different temperatures from 25°C to 150°C for incoming electron energy of 1 MeV and pH value of 7.

In this study, material balance tests between the reducing species and oxidizing species were performed to verify the results. G-values for e^-_{aq}, H_2, $H^\bullet$, $^\bullet OH$, H_2O_2 and HO_2 at different temperatures from 25°C to 150°C were calculated according to the material balance Equations 3.4, 3.5 and 3.6, with a pH value of 7, incoming electron energy of 1 MeV and cut time of 1 μs. As presented in Table 3.1, the material balance tests were satisfied within 0.44% difference.

Physical parameter	**Material balance**
Temperature (°C)	| G_{red} - G_{ox} |
25	0.11%
50	0.21%
75	0.31%
100	0.31%
125	0.24%
150	0.44%

Table 3.1: Material balance tests between the primary species at different temperatures from 25°C to 150°C, with pH value of 7, the energy of 1 MeV and cut time of 1 μs.

3.4.2 Effect of pH Values on G-values for Reactive Species

Figure 3.4 shows the G(e^-_{aq}) and G(e^-_{aq} + $H^\bullet$) at different pH values from 5 to 9 simulated in this work. The results were compared with the published pulse radiolysis experimental results (2; 77) and simulation results from Monte Carlo track structure codes IONLYS-IRT (17), IONLYS-TRACION and IONLYS-TRACELE (18). The G(e^-_{aq} + $H^\bullet$) were also presented in this figure to fairly compare with experimental data. The G(e^-_{aq}) at all simulated pH values were: 2.10 (pH = 5), 2.54 (pH = 6), 2.59 (pH = 7), 2.59 (pH = 8) and 2.60 (pH = 9). In this work, the uncertainties of the pH-dependent G(e^-_{aq}) were less than 0.19%. The trend of the simulated G(e^-_{aq}) was also in good agreement with the published data.

As can be seen in Figure 3.4, our results for all the simulated pH values agreed well with experimental data within 0.52% ± 0.18% to 3.19% ± 0.19% except at pH of 5 (2; 77). For pH of 5, the difference between our simulated result and experimental data from Sprinks and Woods (1990) (2) was 15.99% ± 0.16%. Overall, considering additions of solutes in determining the yield of radiolytic species, and thereby difficulties in controlling the pH values (78; 79), the agreements are acceptable. Regarding simulation results performed with other code packages, our results agreed with the data within 4.40% ± 0.15% to 5.53% ± 0.16% (17; 18). In the acid conditions, hydrogen ion (H^+), which can react with e^-_{aq} and produce $H^\bullet$, are significantly produced, resulting a low yield of e^-_{aq} and a high yield of $^\bullet OH$ (1; 2; 78). In the pH range between 4 and 7, the $G(e^-_{aq} + H^\bullet)$ kept constant and were independent of the pH values. This can be explained by the fact that the main reaction of e^-_{aq} in this pH range is with the H^+, which converts the H^+ to $H^\bullet$ (17). At lower pH values, the reaction rate constant of the e^-_{aq} recombination also increases (80).

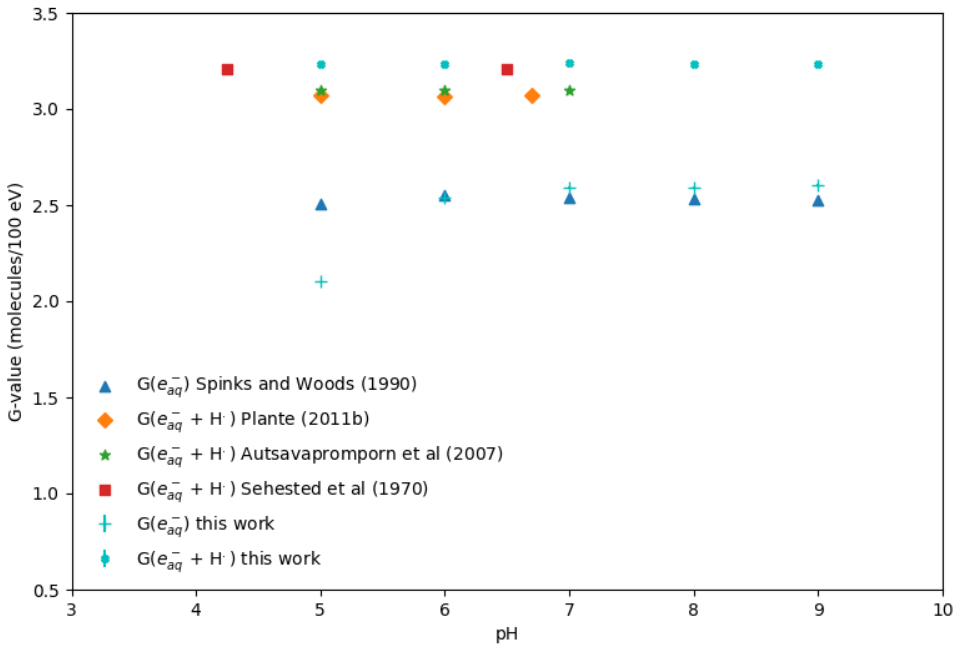

Figure 3.4: G(e^-_{aq}) and G(e^-_{aq} + H$^\bullet$) at different pH values from 5 to 9 simulated in this work and the comparison with published values. The results were compared with the published pulse radiolysis experimental results (2; 77) and simulation results from Monte Carlo track structure codes IONLYS-IRT (17), IONLYS-TRACION and IONLYS-TRACELE (18).

Figure 3.5 shows G-values for oxidizing species G($^\bullet$OH) and G(H_2O_2) at different pH values from 5 to 9 simulated in this work. The results were compared with the published experimental results (2) and simulation results from Monte Carlo track structure codes IONLYS-IRT (17), IONLYS-TRACION and IONLYS-TRACELE (18). The observed trends in G($^\bullet$OH) and G(H_2O_2) align well with those reported in the published work. The G($^\bullet$OH) kept constant in the pH range from 4 to 7 and increased with lower pH values. This is

because, within the pH range of 4 to 7, the reaction involving e^-_{aq} and H^+ resulting in the formation of $H^\bullet$, which is the opposite of scavenging capacity, happens around the same time as the completion of spur expansion. Once the reaction $e^-_{aq} + H^+ \rightarrow H^\bullet$ takes place, the majority of the initial events in the spur expansion process have already occurred, leading to the generation of most of the reactive species (18).

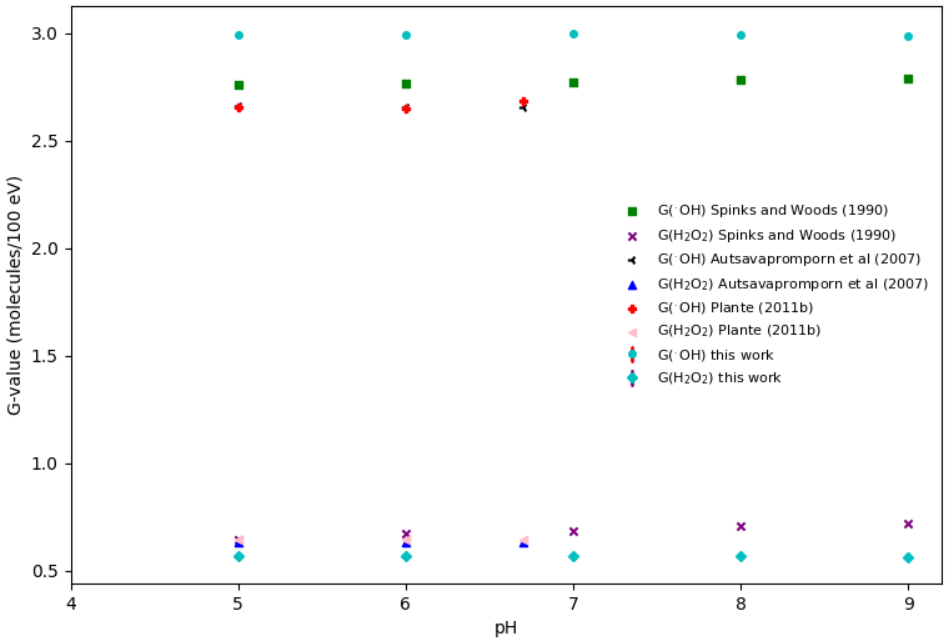

Figure 3.5: G($^\bullet$OH) and G(H_2O_2) at different pH values from 5 to 9 simulated in this work and comparison with the published work. The results were compared with the published experimental results (2) and simulation results from Monte Carlo track structure codes IONLYS-IRT (17), IONLYS-TRACION and IONLYS-TRACELE (18).

Figure 3.6 shows the time-evolution of G-values for different generated reactive species at different pH values from 5 to 9. Uncertainties for G($H^\bullet$), G(H_2), G(H_2O_2), G($^\bullet$OH) and

G(OH^-) at different pH values were within 0.32%.

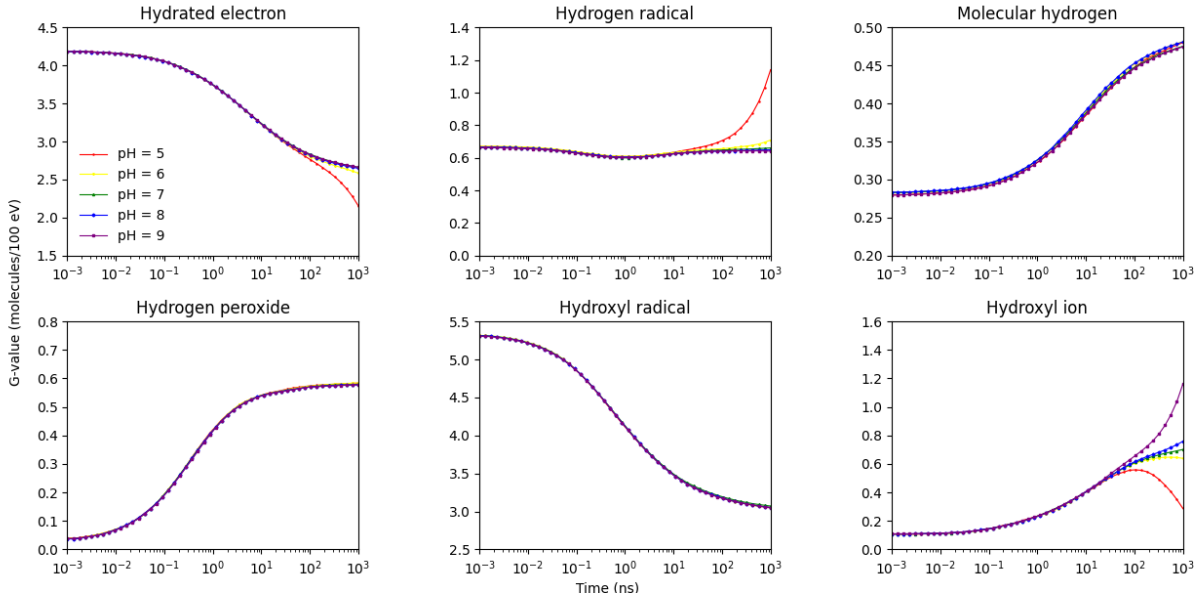

Figure 3.6: Time-evolution of G-values for generated reactive species at different pH values from 5 to 9 with the incoming electron energy of 1 MeV and temperature of 25°C.

The material balance equations were also calculated at different pH values. The results are presented in Table 3.2. The material balance tests were satisfied within 0.19% for pH values of 5, 6, 7, 8, and 9.

Physical parameter	**Material balance**
pH values	$\mid G_{red} - G_{ox} \mid$
5	0.19%
6	0.11%
7	0.11%
8	0.07%
9	0.07%

Table 3.2: Material balance tests between the primary species at different pH values from 5 to 9, with the temperature of 25°C, the incoming electron energy of 1 MeV, and cut time of 1 μs.

3.4.3 Impact

In this project, temperature-dependent scaling functions for the chemical parameters were integrated into the GEANT4-DNA. The GEANT4-DNA was updated to automatically change the chemical parameters based on published databases. The users can use the IRT method with different input chemical parameters. At room temperature and neutral pH, the functions converge to the default GEANT4-DNA chemical parameters.

Accurate knowledge of G-values under correct temperatures and pH values is important in many fields such as studying the biological damage caused by both conventional (81) and FLASH radiation (82). In addition, radiolysis of water is important in the field of dosimetry

such as water calorimetry (83) and e^-_{aq} dosimetry (16; 84) as well as in nuclear reactor technology (85; 86; 87). In e^-_{aq} dosimetry, accurate determination of G(e^-_{aq}) is important to obtain accurate absorbed dose measured with the e^-_{aq} dosimeter prototype (16).

3.4.4 Limitations of the Work and Future Study

In this work, changes in temperatures and pH values were considered to be independent events. However, there does exist a dependency between temperatures and pH values. The definition of pH is based on the amount of H^+ available in the solution. The relationship between pH and H^+ concentration can be expressed as pH = - $\log_{10}$ $[H^+]/mol/L$. The self-dissociation activity of water increases with increasing temperature (88; 89). Moreover, to investigate the effect of pH value on the yields, ionic strength is expected to affect media with high acidity. Those scenarios were not simulated/considered in this work. In future work, the relationship between temperature and pH will be considered and added to the GEANT4-DNA code. Also, further validation using higher LET is required.

3.5 Conclusions

In this work, modifications to the IRT method were successfully added to the GEANT4-DNA source code to simulate G-values for reactive species produced in water radiolysis. G-values for e^-_{aq}, $H^\bullet$, H_2, H_2O_2, $^\bullet OH$ and OH^- for different physical parameters were obtained and analyzed. Our temperature-dependent results agreed with experimental data within 0.64%

to 9.79%, and with simulated data within 3.52% to 12.47%. The pH-dependent results agreed well with experimental data within 0.52% to 3.19% except at a pH of 5 (15.99%) and with simulated data within 4.40% to 5.53%. The uncertainties were below ± 0.20%. Overall our results agreed better with experimental than simulation data. The G-values for the reactive species simulated were consistent with or could be explained by the conclusions drawn in published work.

Acknowledgements

This research was conducted as part of the activities of MEDTEQ+, thanks to the financial support of the Ministry of Economy and Innovation - PSOv2b program, cofounded by TransMedTech (Canada First Research Excellence Fund), Mitacs, the MUHC Foundation, and Varian Medical Systems. Funding from Canada Research Chairs Program (grant # 252135) is acknowledged. Special thanks to Liam Carroll and Alaina Bui for their help with the introduction to Geant4.

Bibliography

[1] G. V. Buxton, C. L. Greenstock, W. P. Helman, and A. B. Ross, "Critical review of rate constants for reactions of hydrated electrons, hydrogen atoms and hydroxyl radicals

($^{\bullet}$oh/$^{\bullet}$o^{-} in aqueous solution," *Journal of physical and chemical reference data*, vol. 17, no. 2, pp. 513–886, 1988.

[2] J. W. Spinks and R. J. Woods, "An introduction to radiation chemistry," 1990.

[3] A. Bui, H. Bekerat, L. Childress, J. Sankey, J. Seuntjens, and S. A. Enger, "Effects of incoming particle energy and cluster size on the g-value of hydrated electrons," *Physica Medica*, vol. 107, p. 102540, 2023.

[4] I. G. DRAGANIĆ and Z. D. DRAGANIĆ, *The radiation chemistry of water*, vol. 26. Elsevier, 1971.

[5] S. Le Caër, "Water radiolysis: influence of oxide surfaces on h_2 production under ionizing radiation," *Water*, vol. 3, no. 1, pp. 235–253, 2011.

[6] D. C. Walker, "The hydrated electron," *Quarterly Reviews, Chemical Society*, vol. 21, no. 1, pp. 79–108, 1967.

[7] M.-A. Hervé du Penhoat, T. Goulet, Y. Frongillo, M.-J. Fraser, P. Bernat, and J.-P. Jay-Gerin, "Radiolysis of liquid water at temperatures up to 300°c: A monte carlo simulation study," *The Journal of Physical Chemistry A*, vol. 104, no. 50, pp. 11757–11770, 2000.

[8] M. Burton, "Radiation chemistry.," *The Journal of Physical Chemistry*, vol. 51, no. 2, pp. 611–625, 1947.

[9] N. Lampe, M. Karamitros, V. Breton, J. M. Brown, I. Kyriakou, D. Sakata, D. Sarramia, and S. Incerti, "Mechanistic dna damage simulations in geant4-dna part 1: A parameter study in a simplified geometry," *Physica Medica*, vol. 48, pp. 135–145, 2018.

[10] C. Villagrasa, S. Meylan, G. Gonon, G. Gruel, U. Giesen, M. Bueno, and H. Rabus, "Geant4-dna simulation of dna damage caused by direct and indirect radiation effects and comparison with biological data.," in *EPJ web of conferences*, vol. 153, p. 04019, EDP Sciences, 2017.

[11] D. Sakata, N. Lampe, M. Karamitros, I. Kyriakou, O. Belov, M. A. Bernal, D. Bolst, M.-C. Bordage, V. Breton, J. M. Brown, *et al.*, "Evaluation of early radiation dna damage in a fractal cell nucleus model using geant4-dna," *Physica Medica*, vol. 62, pp. 152–157, 2019.

[12] R. H. Schuler and A. O. Allen, "Yield of the ferrous sulfate radiation dosimeter: an improved cathode-ray determination," *The Journal of Chemical Physics*, vol. 24, no. 1, pp. 56–59, 1956.

[13] H. S. Judeikis, H. Hedgpeth, and S. Siegel, "Free radical yields in polytetrafluoroethylene as the basis for a radiation dosimeter," *Radiation research*, vol. 35, no. 2, pp. 247–262, 1968.

[14] E. Hart and E. Fielden, "The hydrated electron dosimeter," 1970.

[15] E. J. Hart and J. W. Boag, "Absorption spectrum of the hydrated electron in water and in aqueous solutions," *Journal of the American Chemical Society*, vol. 84, no. 21, pp. 4090–4095, 1962.

[16] J. Mégrourèche, "Development of a hydrated electron dosimeter for radiotherapy applications: a proof of concept," 2020.

[17] N. Autsavapromporn, J. Meesungnoen, I. Plante, and J.-P. Jay-Gerin, "Monte carlo simulation study of the effects of acidity and let on the primary free-radical and molecular yields of water radiolysis-application to the fricke dosimeter," *Canadian journal of chemistry*, vol. 85, no. 3, pp. 214–229, 2007.

[18] I. Plante, "A monte-carlo step-by-step simulation code of the non-homogeneous chemistry of the radiolysis of water and aqueous solutions—part ii: calculation of radiolytic yields under different conditions of let, ph, and temperature," *Radiation and environmental biophysics*, vol. 50, no. 3, pp. 405–415, 2011.

[19] S. Yamashita, Y. Katsumura, M. Lin, Y. Muroya, T. Miyazaki, and T. Murakami, "Water radiolysis with heavy ions of energies up to 28 gev.: 1. measurements of primary g values as track segment yields," *Radiation Physics and Chemistry*, vol. 77, no. 4, pp. 439–446, 2008.

[20] S. Uehara and H. Nikjoo, "Monte carlo simulation of water radiolysis for low-energy charged particles," *Journal of radiation research*, vol. 47, no. 1, pp. 69–81, 2006.

[21] J. A. LaVerne, I. Štefanić, and S. M. Pimblott, "Hydrated electron yields in the heavy ion radiolysis of water," *The Journal of Physical Chemistry A*, vol. 109, no. 42, pp. 9393–9401, 2005.

[22] B. Rudek, A. McNamara, J. Ramos-Méndez, H. Byrne, Z. Kuncic, and J. Schuemann, "Radio-enhancement by gold nanoparticles and their impact on water radiolysis for x-ray, proton and carbon-ion beams," *Physics in Medicine & Biology*, vol. 64, no. 17, p. 175005, 2019.

[23] S. Sanguanmith, J. Meesungnoen, Y. Muroya, M. Lin, Y. Katsumura, and J.-P. Jay-Gerin, "On the spur lifetime and its temperature dependence in the low linear energy transfer radiolysis of water," *Physical Chemistry Chemical Physics*, vol. 14, no. 48, pp. 16731–16736, 2012.

[24] M. S. Kreipl, W. Friedland, and H. G. Paretzke, "Time-and space-resolved monte carlo study of water radiolysis for photon, electron and ion irradiation," *Radiation and environmental biophysics*, vol. 48, no. 1, pp. 11–20, 2009.

[25] S. Uehara, L. Toburen, and H. Nikjoo, "Development of a monte carlo track structure code for low-energy protons in water," *International journal of radiation biology*, vol. 77, no. 2, pp. 139–154, 2001.

[26] D. Boscolo, M. Krämer, M. Durante, M. Fuss, and E. Scifoni, "Trax-chem: A pre-

chemical and chemical stage extension of the particle track structure code trax in water targets," *Chemical Physics Letters*, vol. 698, pp. 11–18, 2018.

[27] B. Grosswendt, V. Conte, and P. Colautti, "An upgraded track structure model: experimental validation," *Radiation protection dosimetry*, vol. 161, no. 1-4, pp. 464–468, 2014.

[28] A. Valota, F. Ballarini, W. Friedland, P. Jacob, A. Ottolenghi, and H. Paretzke, "Modelling study on the protective role of oh radical scavengers and dna higher-order structures in induction of single-and double-strand break by gamma-radiation," *International journal of radiation biology*, vol. 79, no. 8, pp. 643–653, 2003.

[29] H. Nikjoo, S. Uehara, D. Emfietzoglou, and F. Cucinotta, "Track-structure codes in radiation research," *Radiation Measurements*, vol. 41, no. 9-10, pp. 1052–1074, 2006.

[30] S. Incerti, G. Baldacchino, M. Bernal, R. Capra, C. Champion, Z. Francis, P. Gueye, A. Mantero, B. Mascialino, P. Moretto, *et al.*, "The geant4-dna project," *International Journal of Modeling, Simulation, and Scientific Computing*, vol. 1, no. 02, pp. 157–178, 2010.

[31] M. A. Bernal, M. C. Bordage, J. M. C. Brown, M. Davídková, E. Delage, Z. El Bitar, S. A. Enger, Z. Francis, S. Guatelli, V. N. Ivanchenko, *et al.*, "Track structure modeling in liquid water: A review of the geant4-dna very low energy extension of the geant4 monte carlo simulation toolkit," *Physica Medica*, vol. 31, no. 8, pp. 861–874, 2015.

[32] S. Incerti, I. Kyriakou, M. Bernal, M. Bordage, Z. Francis, S. Guatelli, V. Ivanchenko, M. Karamitros, N. Lampe, S. B. Lee, *et al.*, "Geant4-dna example applications for track structure simulations in liquid water: A report from the geant4-dna project," *Medical physics*, vol. 45, no. 8, pp. e722–e739, 2018.

[33] S. Incerti, A. Ivanchenko, M. Karamitros, A. Mantero, P. Moretto, H. Tran, B. Mascialino, C. Champion, V. Ivanchenko, M. Bernal, *et al.*, "Comparison of geant4 very low energy cross section models with experimental data in water," *Medical physics*, vol. 37, no. 9, pp. 4692–4708, 2010.

[34] I. Plante, "A monte–carlo step-by-step simulation code of the non-homogeneous chemistry of the radiolysis of water and aqueous solutions. part i: theoretical framework and implementation," *Radiation and environmental biophysics*, vol. 50, no. 3, pp. 389–403, 2011.

[35] W.-G. Shin, J. Ramos-Mendez, B. Faddegon, H. Tran, C. Villagrasa, Y. Perrot, S. Okada, M. Karamitros, D. Emfietzoglou, I. Kyriakou, *et al.*, "Evaluation of the influence of physical and chemical parameters on water radiolysis simulations under mev electron irradiation using geant4-dna," *Journal of Applied Physics*, vol. 126, no. 11, p. 114301, 2019.

[36] M. Karamitros, S. Luan, M. A. Bernal, J. Allison, G. Baldacchino, M. Davidkova, Z. Francis, W. Friedland, V. Ivantchenko, A. Ivantchenko, *et al.*, "Diffusion-controlled

reactions modeling in geant4-dna," *Journal of Computational Physics*, vol. 274, pp. 841–882, 2014.

[37] J. Ramos-Méndez, L. N. Burigo, R. Schulte, C. Chuang, and B. Faddegon, "Fast calculation of nanodosimetric quantities in treatment planning of proton and ion therapy," *Physics in Medicine & Biology*, vol. 63, no. 23, p. 235015, 2018.

[38] V. Ivanchenko, J. Apostolakis, A. Bagulya, H. B. Abdelouahed, R. Black, A. Bogdanov, H. Burkhard, S. Chauvie, G. A. P. Cirrone, G. Cuttone, *et al.*, "Recent improvements in geant4 electromagnetic physics models and interfaces," *Progress in nuclear science and technology*, vol. 2, pp. 898–903, 2011.

[39] J. Ramos-Méndez, W.-g. Shin, M. Karamitros, J. Domínguez-Kondo, N. H. Tran, S. Incerti, C. Villagrasa, Y. Perrot, V. Štěpán, S. Okada, *et al.*, "Independent reaction times method in geant4-dna: Implementation and performance," *Medical physics*, vol. 47, no. 11, pp. 5919–5930, 2020.

[40] P. Clifford, N. J. Green, and M. J. Pilling, "Stochastic model based on pair distribution functions for reaction in a radiation-induced spur containing one type of radical," *The Journal of Physical Chemistry*, vol. 86, no. 8, pp. 1318–1321, 1982.

[41] P. Clifford, N. J. Green, and M. J. Pilling, "Monte carlo simulation of diffusion and reaction in radiation-induced spurs. comparisons with analytic models," *The Journal of Physical Chemistry*, vol. 86, no. 8, pp. 1322–1327, 1982.

[42] P. Clifford, N. J. Green, M. J. Oldfield, M. J. Pilling, and S. M. Pimblott, "Stochastic models of multi-species kinetics in radiation-induced spurs," *Journal of the Chemical Society, Faraday Transactions 1: Physical Chemistry in Condensed Phases*, vol. 82, no. 9, pp. 2673–2689, 1986.

[43] T. Goulet, M.-J. Fraser, Y. Frongillo, and J.-P. Jay-Gerin, "On the validity of the independent reaction times approximation for the description of the nonhomogeneous kinetics of liquid water radiolysis," *Radiation Physics and Chemistry*, vol. 51, no. 1, pp. 85–91, 1998.

[44] H. C. Berg, "Random walks in biology," in *Random Walks in Biology*, Princeton University Press, 1993.

[45] N. J. Green, M. J. Pilling, S. M. Pimblott, and P. Clifford, "Stochastic models of diffusion-controlled ionic reactions-induced spurs. 2. low-permittivity solvents," *The Journal of Physical Chemistry*, vol. 93, no. 24, pp. 8025–8031, 1989.

[46] P. Clifford, N. J. Green, and M. J. Pilling, "Analysis of the debye-smoluchowski equation. approximations for high-permittivity solvents," *The Journal of Physical Chemistry*, vol. 88, no. 18, pp. 4171–4176, 1984.

[47] J. Meesungnoen, J.-P. Jay-Gerin, A. Filali-Mouhim, and S. Mankhetkorn, "Low-energy electron penetration range in liquid water," *Radiation research*, vol. 158, no. 5, pp. 657–660, 2002.

[48] A. Mozumder, *Fundamentals of radiation chemistry*. Elsevier, 1999.

[49] N. Green, M. Pilling, S. Pimblott, and P. Clifford, "Stochastic modeling of fast kinetics in a radiation track," *Journal of Physical Chemistry*, vol. 94, no. 1, pp. 251–258, 1990.

[50] H. Sano and M. Tachiya, "Partially diffusion-controlled recombination," *The Journal of Chemical Physics*, vol. 71, no. 3, pp. 1276–1282, 1979.

[51] A. J. Elliot and D. R. McCracken, "Computer modelling of the radiolysis in an aqueous lithium salt blanket: Suppression of radiolysis by addition of hydrogen," *Fusion engineering and design*, vol. 13, no. 1, pp. 21–27, 1990.

[52] B. Pastina and J. A. LaVerne, "Effect of molecular hydrogen on hydrogen peroxide in water radiolysis," *The Journal of Physical Chemistry A*, vol. 105, no. 40, pp. 9316–9322, 2001.

[53] J. Ramos-Méndez, O. García-García, J. Domínguez-Kondo, J. A. LaVerne, J. Schuemann, E. Moreno-Barbosa, and B. Faddegon, "Topas-nbio simulation of temperature-dependent indirect dna strand break yields," *Physics in Medicine & Biology*, vol. 67, no. 14, p. 145007, 2022.

[54] A. Elliot, "Rate constants and g-values for the simulation of the radiolysis of light water over the range 0-300°c," tech. rep., Atomic Energy of Canada Ltd., 1994.

[55] W. G. Burns and W. R. Marsh, "Radiation chemistry of high-temperature (300–410°c)

water. part 1.-reducing products from gamma radiolysis," *Journal of the Chemical Society, Faraday Transactions 1: Physical Chemistry in Condensed Phases*, vol. 77, no. 1, pp. 197–215, 1981.

[56] A. Elliot and D. Bartels, "The reaction set, rate constants and g-values for the simulation of the radiolysis of light water over the range 20° to 350°c based on information available in 2008," tech. rep., Atomic Energy of Canada Limited, 2009.

[57] K. Schmidt, P. Han, and D. Bartels, "Radiolytic yields of the hydrated electron from transient conductivity. improved calculation of the hydrated electron diffusion coefficient and analysis of some diffusion-limited $(e^-)_{aq}$ reaction rates," *The Journal of Physical Chemistry*, vol. 99, no. 26, pp. 10530–10539, 1995.

[58] D. T. Kallikragas, A. Y. Plugatyr, and I. M. Svishchev, "High temperature diffusion coefficients for o_2, h_2, and oh in water, and for pure water," *Journal of Chemical & Engineering Data*, vol. 59, no. 6, pp. 1964–1969, 2014.

[59] T. F. Irvine and J. P. Hartnett, *Steam and Air Tables in SI Units: Including Data for Other Substances with a Separate Mollier Chart for Steam*. Hemisphere Pub, 1976.

[60] J. J. de Pablo, J. M. Prausnitz, H. J. Strauch, and P. T. Cummings, "Molecular simulation of water along the liquid–vapor coexistence curve from 25°c to the critical point," *The Journal of chemical physics*, vol. 93, no. 10, pp. 7355–7359, 1990.

[61] B. A. Bauer and S. Patel, "Properties of water along the liquid-vapor coexistence curve via molecular dynamics simulations using the polarizable tip4p-qdp-lj water model," *The Journal of Chemical Physics*, vol. 131, no. 8, p. 084709, 2009.

[62] P. Linstorm, "Nist chemistry webbook, nist standard reference database number 69," *J. Phys. Chem. Ref. Data, Monograph*, vol. 9, pp. 1–1951, 1998.

[63] I. Plante and L. Devroye, "Considerations for the independent reaction times and step-by-step methods for radiation chemistry simulations," *Radiation Physics and Chemistry*, vol. 139, pp. 157–172, 2017.

[64] "G4dnachemistrymanager class reference." Website. `https://apc.u-paris.fr/~franco/g4doxy/html/classG4DNAChemistryManager.html`.

[65] V. Cobut, Y. Frongillo, J. Patau, T. Goulet, M. Fraser, and J. Jay-Gerin, "Monte carlo simulation of fast electron and proton tracks in liquid water-i. physical and physicochemical aspects," *Radiation Physics and Chemistry*, vol. 51, no. 3, pp. 229–244, 1998.

[66] W.-G. Shin, J. Ramos-Mendez, N. H. Tran, S. Okada, Y. Perrot, C. Villagrasa, and S. Incerti, "Geant4-dna simulation of the pre-chemical stage of water radiolysis and its impact on initial radiochemical yields," *Physica Medica*, vol. 88, pp. 86–90, 2021.

[67] W. G. Shin, *Development and application of the Geant4-DNA toolkit for the simulation of radiobiological effects at the sub-cellular scale*. PhD thesis, Bordeaux, 2020.

[68] C. Champion, S. Incerti, H. Aouchiche, and D. Oubaziz, "A free-parameter theoretical model for describing the electron elastic scattering in water in the geant4 toolkit," *Radiation Physics and Chemistry*, vol. 78, no. 9, pp. 745–750, 2009.

[69] A. J. Elliot and D. C. Ouellette, "Temperature dependence of g values for h_2o and d_2o irradiated with low linear energy transfer radiation," *Journal of the Chemical Society, Faraday Transactions*, vol. 89, no. 8, pp. 1193–1197, 1993.

[70] S. M. Pimblott and J. A. LaVerne, "Effect of electron energy on the radiation chemistry of liquid water," *Radiation research*, vol. 150, no. 2, pp. 159–169, 1998.

[71] M. Karamitros, A. Mantero, S. Incerti, W. Friedland, G. Baldacchino, P. Barberet, M. Bernal, R. Capra, C. Champion, Z. El Bitar, *et al.*, "Modeling radiation chemistry in the geant4 toolkit," *Prog. Nucl. Sci. Technol*, vol. 2, pp. 503–508, 2011.

[72] A. O. Allen, *The radiation chemistry of water and aqueous solutions*. van Nostrand, 1961.

[73] D. G. Edelen, "Mass balance laws and the decomposition, evolution and stability of chemical systems," *International Journal of Engineering Science*, vol. 13, no. 9-10, pp. 763–784, 1975.

[74] M. Lin, Y. Katsumura, Y. Muroya, H. He, G. Wu, Z. Han, T. Miyazaki, and H. Kudo, "Pulse radiolysis study on the estimation of radiolytic yields of water decomposition products in high-temperature and supercritical water: use of methyl viologen as a scavenger," *The Journal of Physical Chemistry A*, vol. 108, no. 40, pp. 8287–8295, 2004.

[75] A. JohnáElliot *et al.*, "Temperature dependence of the rate constant for the reaction e^-_{aq} + oh in water up to 150°c," *Journal of the Chemical Society, Faraday Transactions*, vol. 90, no. 6, pp. 837–841, 1994.

[76] A. J. Elliot, M. P. Chenier, D. C. Ouellette, and V. T. Koslowsky, "Temperature dependence of g values for aqueous solutions irradiated with 23 mev $^2h^+$ and 157 mev $^7li^{3+}$ ion beams," *The Journal of Physical Chemistry*, vol. 100, no. 21, pp. 9014–9020, 1996.

[77] K. Sehested, H. Corfitzen, and H. Fricke, "Cobalt-60 γ-ray radiolysis of aqueous solutions of h_2 + o_2. determination of $g_{e^-_{aq}}$ + g_h at ph 0.46-6.5," *The Journal of Physical Chemistry*, vol. 74, no. 1, pp. 211–213, 1970.

[78] N. Getoff, "Radiation-induced degradation of water pollutants—state of the art," *Radiation Physics and Chemistry*, vol. 47, no. 4, pp. 581–593, 1996.

[79] N. Getoff, "Advancements of radiation induced degradation of pollutants in drinking

and waste water," *International Journal of Radiation Applications and Instrumentation. Part A. Applied Radiation and Isotopes*, vol. 40, no. 7, pp. 585–594, 1989.

[80] T. W. Marin, K. Takahashi, C. D. Jonah, S. D. Chemerisov, and D. M. Bartels, "Recombination of the hydrated electron at high temperature and pressure in hydrogenated alkaline water," *The Journal of Physical Chemistry A*, vol. 111, no. 45, pp. 11540–11551, 2007.

[81] J. Ramos-Méndez, J. LaVerne, N. Domínguez-Kondo, J. Milligan, V. Štěpán, K. Stefanová, Y. Perrot, C. Villagrasa, W. Shin, S. Incerti, *et al.*, "Topas-nbio validation for simulating water radiolysis and dna damage under low-let irradiation," *Physics in Medicine & Biology*, vol. 66, no. 17, p. 175026, 2021.

[82] D. Boscolo, E. Scifoni, M. Durante, M. Krämer, and M. C. Fuss, "May oxygen depletion explain the flash effect? a chemical track structure analysis," *Radiotherapy and Oncology*, vol. 162, pp. 68–75, 2021.

[83] C. Ross and N. Klassen, "Water calorimetry for radiation dosimetry," *Physics in Medicine & Biology*, vol. 41, no. 1, p. 1, 1996.

[84] E. Fielden and E. J. HART, "Hydrated electron and thermoluminescent dosimetry of pulsed x-ray beams," ACS Publications, 1968.

[85] D. McCracken, K. Tsang, and P. Laughton, "Aspects of the physics and chemistry of water radiolysis by fast neutrons and fast electrons in nuclear reactors," 1998.

[86] D. M. Bartels, J. Henshaw, and H. E. Sims, "Modeling the critical hydrogen concentration in the aecl test reactor," *Radiation Physics and Chemistry*, vol. 82, pp. 16–24, 2013.

[87] K. Kanjana, K. S. Haygarth, W. Wu, and D. M. Bartels, "Laboratory studies in search of the critical hydrogen concentration," *Radiation Physics and Chemistry*, vol. 82, pp. 25–34, 2013.

[88] F. H. Sweeton, R. Mesmer, and C. Baes, "Acidity measurements at elevated temperatures. vii. dissociation of water," *Journal of Solution Chemistry*, vol. 3, no. 3, pp. 191–214, 1974.

[89] P. L. Geissler, C. Dellago, D. Chandler, J. Hutter, and M. Parrinello, "Autoionization in liquid water," *Science*, vol. 291, no. 5511, pp. 2121–2124, 2001.

Chapter 4

Discussion

In this section, a summary of the findings, limitations and future work for the modification of GEANT4-DNA simulation of G-values for the radiolytic species is discussed. An overall discussion of the thesis as well as the future directions, are also presented in this section.

4.1 Modifying GEANT4-DNA to Enable Simulation of G-values at Different Temperatures and pH Values

Water molecules can be decomposed by interacting with ionizing radiation (118). The short-lived products of this process are e^-_{aq}, as described in Section 2.2.2, as well as many other reactive species ($^{\bullet}OH$, H_3O^+,H_2, H_2O_2, $H^{\bullet}$, etc.). G-values for these different reactive species

depend on many factors, such as the temperature and pH value of the solution (107; 119; 120).

Sanguanmith *et. al* (2013) (121) simulated and analyzed time-dependent G($^{\bullet}$OH) for low-LET radiolysis from 25°C to 250°C with the IONLYS-IRT Monte Carlo track structure code. Sultana *et. al* (2020) (122) also used IONLYS-IRT to simulate G-values for generated species from water radiolysis. Though IONLYS-IRT code can be used to simulate radiolysis at varying temperatures, it is not an open-source code and cannot be accessed.

In this thesis, the open-source GEANT4-DNA source code was further developed to benefit a larger scientific community and our own applications within the research group. The code was modified by adding temperature-dependent polynomials (1; 2; 3; 4; 5; 123) and pH-dependent concentrations (107) to obtain G-values for reactive species produced in water radiolysis at different temperatures (from 25°C to 150°C) and pH values (from 5 to 9). Simulations of G-values for the produced species were performed and compared with published data (1; 65; 107; 119; 124; 125; 126) for benchmarking purposes. The uncertainties of the temperature and pH-dependent G-values were less than 0.32%. Our temperature-dependent results were consistent with experimental data within 0.64% to 9.79% and with simulated data within 3.52% to 12.47%. The pH-dependent results were consistent with experimental data within 0.52% to 3.19% except at pH of 5 (15.99%) and with simulated data within 4.40% to 5.53%. The uncertainties were below ±0.20%. Overall our results agreed better with experimental than simulation data.

4.2 Importance of Water Radiolysis and Accurate G-values

Accurate knowledge of G-values under correct experimental conditions (i.e., temperature and pH value of the solution) is essential in many areas, such as investigations of the indirect DNA damage, radiation dosimetry and nuclear reactor technology (127; 128). For low-LET radiation, almost two-thirds of the radiation-induced DNA damages are indirect, resulting from the interaction between produced reactive free species and radiation-sensitive components of the cell, such as DNA and RNA. The formed free radicals in water radiolysis that contribute to damaging the biological systems are mostly $^{\bullet}OH$, e^{-}_{aq} and $H^{\bullet}$ (27). Among these, $^{\bullet}OH$ is the most reactive species. It diffuses, reaches and reacts with radiation-sensitive components of the cell (129). The $^{\bullet}OH$ attacks the DNA backbone, bases, and nucleoproteins, causing base lesions, single-strand breaks, double-strand breaks, and DNA protein cross-links with different mechanisms (28; 29). Lipid peroxidation is also caused by $^{\bullet}OH$ abstracting a hydrogen atom from a polyunsaturated lipid molecule. The $^{\bullet}OH$ has a short lifetime of 10^{-9} s. The e^{-}_{aq} and $H^{\bullet}$ also contribute to DNA damage by mainly causing base lesions (30). The G-values for radiolytic species are dependent on temperature and pH values. Therefore temperature and pH have a potential influence on the formation and repair of radiation-induced DNA strand breaks and DNA protein cross-links in irradiated partially hypoxic or fully hypoxic cells (130). As temperature

increases, G-values for both e^-_{aq} and $^{\bullet}OH$ at about 10^{-12} s slightly increase. At after 10^{-11} s, G-values for both e^-_{aq} and $^{\bullet}OH$ decrease with time (131). As shown in Figure 3.3, from 10^{-12} s to 10^{-6} s, G($^{\bullet}OH$) increases with temperature. Figure 3.6 presents the pH-dependency of the yield of radiolytic species. As pH increases, the scavenger power of the Reaction R10, which is the product of reaction rate constant and the concentration of H^+, decreases. Thus G(e^-_{aq}) increases and G($H^{\bullet}$) decreases. The G($^{\bullet}OH$) keeps consistent.

Recent studies suggest that ultra-high dose-rate (> 40 Gy/s) (FLASH) irradiation can reduce the normal tissue toxicities while maintaining local tumor control (132; 133). This "FLASH effect" is still not fully understood and is under investigation. The updated version of GEANT4-DNA can be used to investigate the impact of radiolytic oxygen depletion, which is one of the theories behind the "FLASH effect" and the role of other reactive species on the cellular response after FLASH irradiation.

For dosimetry, investigation of the response of the e^-_{aq} dosimeter due to the change in temperature is also essential since there exists a temperature difference between patient skin (usually 37°C) and the room temperature (usually 25°C). As presented in Figure 3.1, G(e^-_{aq}) slightly increased with temperature changing from 25°C to 37°C, because the reaction rate constant of Reaction R6 increases less than the diffusion of the species with increasing temperatures. As temperature increases, more e^-_{aq} are available to diffuse out of the spur or to react in the spur. Moreover, the water-based solution is a crucial part of the e^-_{aq} dosimeter prototype. The pH value of the solution has to be properly selected to maximize

the G(e^-_{aq}), resulting in a higher detected absorbance signal. As presented in Figure 3.4, G(e^-_{aq}) increased with increasing pH values. Hence, the knowledge of the pH value of the solution and its effect on the G-values for the e^-_{aq} and other reactive species is fundamental for accurate determination of absorbed dose measurement in e^-_{aq} dosimetry.

Water calorimetry measures the absorbed dose to water from ionizing radiation using the temperature rise produced in water. For accurate dose measurements, a correction factor called heat defect is needed. Heat defect corrects for the radiation-induced chemical changes in water, which causes the measured temperature rise to be greater or smaller than the value corresponding to the complete conversion of the energy absorbed by the water into heat (50; 74). The modified GEANT4-DNA version can be used to calculate the heat defect for water calorimetry.

4.3 Limitations and Future Work

The modified simulation of the water radiolysis with GEANT4-DNA has several limitations. First, the simulations in this work were only performed with electron beams. However, other radiation qualities are also used in radiation dosimetry. For example, the e^-_{aq} dosimeter prototype previously developed by Mégrourèche *et al.* (2020) (39) was performed with both electron and photon beams. Furthermore, GEANT4-DNA only performs simulation for electron interactions for energies up to 1 MeV. Bui *et al.* (2021) (117) studied potential factors affecting G-values and found that G(e^-_{aq}) would remain stable as the incoming electron energy

increases to above 1 MeV. As mentioned in Section 3.4.4, in this work, changes in temperature and pH were considered to be independent events. In future studies, the dependency between temperature and pH needs to be established. The ionic strength should also be considered for scenarios with high acidity. In addition to improvements to the GEANT4-DNA source code, the e^-_{aq} dosimeter previously developed by Mégrourèche *et al.* (2020) (39) will be further improved. Many factors impact the results of the measurements such as contamination of the solution, different optical components and the cavity material. Currently, a basic NaOH solution with a pH value of 11.2±0.1 is used in the prototype. When the solution is exposed to air for a long time, it will react with air molecules, such as CO_2, thereby decreasing the pH value and hence the $G(e^-_{aq})$. The solution can also be contaminated by O_2, which is a scavenger of e^-_{aq}, resulting in a decrease of the lifetime of e^-_{aq}. Air bubbles need to successively be removed from the cavity, otherwise affecting the transmission of the laser in the cavity. The solution enclosed in the cavity needs to be prepared on the same day as the measurements will be performed. It is important to keep the cavity sealed to ensure a clean and contamination-free solution. To increase the concentration of e^-_{aq}, N_2 should be bubbled inside the solution to remove O_2. During the preparation steps, a pH meter and an O_2 meter should be inserted into the solution to monitor the pH value and concentration of the O_2. Both the pH meter and the O_2 meter need to be cleaned with deionized water from the water purification system before use.

Chapter 5

Conclusion

In this project, the GEANT4-DNA source code was modified to obtain the radiation chemical yield (G-value) for different reactive species produced during the water radiolysis for different temperatures and pH values. Our temperature-dependent results agreed with experimental data within 0.64% to 9.79%, and with simulated data within 3.52% to 12.47%. The pH-dependent results agreed well with experimental data within 0.52% to 3.19% except at pH of 5 (15.99%) and with simulated data within 4.40% to 5.53%. The uncertainties were below ±0.20%. Overall our results agreed better with experimental than simulation data. This work enables users to use the IRT method with different input parameters by providing a way to automatically change the chemical parameters. It also benefits our e^-_{aq} dosimeter development by providing the accurate determination of $G(e^-_{aq})$ at specific physical parameters.

Bibliography

[1] A. Elliot and D. Bartels, "The reaction set, rate constants and g-values for the simulation of the radiolysis of light water over the range 20° to 350°c based on information available in 2008," tech. rep., Atomic Energy of Canada Limited, 2009.

[2] A. Elliot, "Rate constants and g-values for the simulation of the radiolysis of light water over the range 0-300°c," tech. rep., Atomic Energy of Canada Ltd., 1994.

[3] W. G. Burns and W. R. Marsh, "Radiation chemistry of high-temperature (300–410°c) water. part 1.-reducing products from gamma radiolysis," *Journal of the Chemical Society, Faraday Transactions 1: Physical Chemistry in Condensed Phases*, vol. 77, no. 1, pp. 197–215, 1981.

[4] D. T. Kallikragas, A. Y. Plugatyr, and I. M. Svishchev, "High temperature diffusion coefficients for o_2, h_2, and oh in water, and for pure water," *Journal of Chemical & Engineering Data*, vol. 59, no. 6, pp. 1964–1969, 2014.

[5] K. Schmidt, P. Han, and D. Bartels, "Radiolytic yields of the hydrated electron from transient conductivity. improved calculation of the hydrated electron diffusion coefficient and analysis of some diffusion-limited $(e^-)_{aq}$ reaction rates," *The Journal of Physical Chemistry*, vol. 99, no. 26, pp. 10530–10539, 1995.

[6] E. B. Podgoršak, "Radiation oncology physics: A handbook for teachers and students.," IAEA; 2005.

[7] E. B. Podgoršak, *Radiation physics for medical physicists*, vol. 1. Springer, 2006.

[8] P. Andreo, D. T. Burns, A. E. Nahum, J. Seuntjens, and F. H. Attix, *Fundamentals of ionizing radiation dosimetry*. John Wiley & Sons, 2017.

[9] "Defining cancer. national cancer institute.." Website, 2014. `https://www.cancer.gov/about-cancer/understanding/what-is-cancer`.

[10] D. E. Gerber, "Targeted therapies: a new generation of cancer treatments," *American family physician*, vol. 77, no. 3, pp. 311–319, 2008.

[11] M. Vanneman and G. Dranoff, "Combining immunotherapy and targeted therapies in cancer treatment," *Nature reviews cancer*, vol. 12, no. 4, pp. 237–251, 2012.

[12] M. Arruebo, N. Vilaboa, B. Sáez-Gutierrez, J. Lambea, A. Tres, M. Valladares, and Á. González-Fernández, "Assessment of the evolution of cancer treatment therapies," *Cancers*, vol. 3, no. 3, pp. 3279–3330, 2011.

[13] T. A Baudino, "Targeted cancer therapy: the next generation of cancer treatment," *Current drug discovery technologies*, vol. 12, no. 1, pp. 3–20, 2015.

[14] C. Stokke, M. Kvassheim, and J. Blakkisrud, "Radionuclides for targeted therapy: Physical properties," *Molecules*, vol. 27, no. 17, p. 5429, 2022.

[15] A. C. Begg, F. A. Stewart, and C. Vens, "Strategies to improve radiotherapy with targeted drugs," *Nature Reviews Cancer*, vol. 11, no. 4, pp. 239–253, 2011.

[16] R. Baskar, K. A. Lee, R. Yeo, and K.-W. Yeoh, "Cancer and radiation therapy: current advances and future directions," *International journal of medical sciences*, vol. 9, no. 3, p. 193, 2012.

[17] P. E. Metcalfe, T. Kron, and P. Hoban, "The physics of radiotherapy x-rays and electrons," 2007.

[18] D. Schulz-Ertner and H. Tsujii, "Particle radiation therapy using proton and heavier ion beams," *Journal of clinical oncology*, vol. 25, no. 8, pp. 953–964, 2007.

[19] M. Durante and J. S. Loeffler, "Charged particles in radiation oncology," *Nature reviews Clinical oncology*, vol. 7, no. 1, pp. 37–43, 2010.

[20] J.-s. Wang, H.-j. Wang, and H.-l. Qian, "Biological effects of radiation on cancer cells," *Military Medical Research*, vol. 5, no. 1, pp. 1–10, 2018.

[21] S. Seltzer, D. Bartlett, D. Burns, G. Dietze, H.-G. Menzel, H. Paretzke, and A. Wambersie, "Fundamental quantities and units for ionizing radiation," *ICRU Journal*, vol. 11, no. 1, p. 1, 2011.

[22] F. H. Attix, *Introduction to radiological physics and radiation dosimetry*. John Wiley & Sons, 2008.

[23] K. M. Prise, "New advances in radiation biology," *Occupational Medicine*, vol. 56, no. 3, pp. 156–161, 2006.

[24] R. Teoule, "Radiation-induced dna damage and its repair," *International Journal of Radiation Biology and Related Studies in Physics, Chemistry and Medicine*, vol. 51, no. 4, pp. 573–589, 1987.

[25] J. A. Reisz, N. Bansal, J. Qian, W. Zhao, and C. M. Furdui, "Effects of ionizing radiation on biological molecules—mechanisms of damage and emerging methods of detection," *Antioxidants & redox signaling*, vol. 21, no. 2, pp. 260–292, 2014.

[26] N. Suntharalingam, E. B. Podgorsak, and J. H. Hendry, "Basic radiobiology," *Radiation oncology physics: A handbook for teachers and students*, pp. 485–504, 2005.

[27] R. S. Feldberg and J. A. Carew, "Water radiolysis products and nucleotide damage in γ-irradiated dna," *International Journal of Radiation Biology and Related Studies in Physics, Chemistry and Medicine*, vol. 40, no. 1, pp. 11–17, 1981.

[28] B. Balasubramanian, W. K. Pogozelski, and T. D. Tullius, "Dna strand breaking by the hydroxyl radical is governed by the accessible surface areas of the hydrogen atoms of the dna backbone," *Proceedings of the National Academy of Sciences*, vol. 95, no. 17, pp. 9738–9743, 1998.

[29] N. L. Oleinick, S. Chiu, N. Ramakrishnan, and L. Y. Xue, "The formation,

identification, and significance of dna-protein cross-links in mammalian cells.," *The British journal of cancer. Supplement*, vol. 8, p. 135, 1987.

[30] S. Steenken, "Purine bases, nucleosides, and nucleotides: aqueous solution redox chemistry and transformation reactions of their radical cations and e^- and oh adducts," *Chemical Reviews*, vol. 89, no. 3, pp. 503–520, 1989.

[31] R. Baskar, J. Dai, N. Wenlong, R. Yeo, and K.-W. Yeoh, "Biological response of cancer cells to radiation treatment," *Frontiers in molecular biosciences*, vol. 1, p. 24, 2014.

[32] F. Ballarini, M. P. Carante, A. Embriaco, and R. L. Ramos, "Effects of ionizing radiation in biomolecules, cells and tissue/organs: basic mechanisms and applications for cancer therapy, medical imaging and radiation protection," *AIMS Biophysics*, vol. 9, no. 2, pp. 108–112, 2022.

[33] *Development of Procedures for In Vivo Dosimetry in Radiotherapy*. No. 8 in Human Health Reports, Vienna: INTERNATIONAL ATOMIC ENERGY AGENCY, 2013.

[34] "Entrance skin dose." website. `https://radiopaedia.org/articles/entrance-skin-dose`.

[35] B. Mijnheer, S. Beddar, J. Izewska, and C. Reft, "In vivo dosimetry in external beam radiotherapy," *Medical physics*, vol. 40, no. 7, p. 070903, 2013.

[36] R. Boellaard, M. Van Herk, and B. Mijnheer, "A convolution model to convert

transmission dose images to exit dose distributions," *Medical physics*, vol. 24, no. 2, pp. 189–199, 1997.

[37] E. Belau, R. Klanner, G. Lutz, W. Maenner, E. Neugebauer, H. Seebrunner, A. Wylie, J. Kemmer, and U. Koetz, "Silicon detectors with 5. mu. m spatial resolution for high energy particles," *Nucl. Instrum. Methods Phys. Res.;(Netherlands)*, vol. 217, no. 1/2, 1983.

[38] E. J. Hart and J. W. Boag, "Absorption spectrum of the hydrated electron in water and in aqueous solutions," *Journal of the American Chemical Society*, vol. 84, no. 21, pp. 4090–4095, 1962.

[39] J. Mégrourèche, "Development of a hydrated electron dosimeter for radiotherapy applications: a proof of concept," 2020.

[40] F. C. Rodrigues-Machado, P. Pestre, V. Dumont, S. Bernard, E. Janitz, L. Scanlon, S. A. Enger, L. Childress, and J. Sankey, "Sideband cavity absorption readout (sidecar) with a robust frequency lock," *Optics Express*, vol. 30, no. 2, pp. 754–767, 2022.

[41] J. K. Baird, G. P. Miller, and N. Li, "The g value in plasma and radiation chemistry," *Journal of applied physics*, vol. 68, no. 7, pp. 3661–3668, 1990.

[42] A. J. Elliot, M. P. Chenier, and D. C. Ouellette, "g-values for γ-irradiated water as a

function of temperature," *Canadian Journal of Chemistry*, vol. 68, no. 5, pp. 712–719, 1990.

[43] M. McEwen, I. El Gamal, E. Mainegra-Hing, and C. Cojocaru, "Determination of the radiation chemical yield (g) for the fricke chemical dosimetry system in photon and electron beams," *National Research Council of Canada*, 2014.

[44] S. Uehara and H. Nikjoo, "Monte carlo simulation of water radiolysis for low-energy charged particles," *Journal of radiation research*, vol. 47, no. 1, pp. 69–81, 2006.

[45] W.-G. Shin, J. Ramos-Mendez, B. Faddegon, H. Tran, C. Villagrasa, Y. Perrot, S. Okada, M. Karamitros, D. Emfietzoglou, I. Kyriakou, *et al.*, "Evaluation of the influence of physical and chemical parameters on water radiolysis simulations under mev electron irradiation using geant4-dna," *Journal of Applied Physics*, vol. 126, no. 11, p. 114301, 2019.

[46] W.-G. Shin, J. Ramos-Mendez, N. H. Tran, S. Okada, Y. Perrot, C. Villagrasa, and S. Incerti, "Geant4-dna simulation of the pre-chemical stage of water radiolysis and its impact on initial radiochemical yields," *Physica Medica*, vol. 88, pp. 86–90, 2021.

[47] K. Baba, T. Kusumoto, S. Okada, R. Ogawara, S. Kodaira, Q. Raffy, R. Barillon, N. Ludwig, C. Galindo, P. Peaupardin, *et al.*, "Quantitative estimation of track segment yields of water radiolysis species under heavy ions around bragg peak energies using geant4-dna," *Scientific Reports*, vol. 11, no. 1, pp. 1–11, 2021.

[48] G. F. Knoll, *Radiation detection and measurement*. John Wiley & Sons, 2010.

[49] J. Izewska and G. Rajan, "Radiation dosimeters," *Radiation oncology physics: a handbook for teachers and students*, pp. 71–99, 2005.

[50] C. Ross and N. Klassen, "Water calorimetry for radiation dosimetry," *Physics in Medicine & Biology*, vol. 41, no. 1, p. 1, 1996.

[51] D. McCammon, "Thermal equilibrium calorimeters–an introduction," in *Cryogenic particle detection*, pp. 1–34, Springer, 2005.

[52] A. Fantom, *Radio frequency & microwave power measurement*. No. 7, IET, 1990.

[53] H. Schrader, "Ionization chambers," *Metrologia*, vol. 44, no. 4, p. S53, 2007.

[54] D. Burns and L. Büermann, "Free-air ionization chambers," *Metrologia*, vol. 46, no. 2, p. S9, 2009.

[55] G. Jayson, B. Parsons, and A. J. Swallow, "The mechanism of the fricke dosimeter," *International Journal for Radiation Physics and Chemistry*, vol. 7, no. 2-3, pp. 363–370, 1975.

[56] L. Schreiner, "Review of fricke gel dosimeters," in *Journal of Physics: Conference Series*, vol. 3, p. 003, IOP Publishing, 2004.

[57] H. Khoury, E. da Silva Jr, K. Mehta, V. de Barros, V. Asfora, P. Guzzo, and A. Parker,

"Alanine-epr as a transfer standard dosimetry system for low energy x radiation," *Radiation Physics and Chemistry*, vol. 116, pp. 147–150, 2015.

[58] S. Pai, I. J. Das, J. F. Dempsey, K. L. Lam, T. J. LoSasso, A. J. Olch, J. R. Palta, L. E. Reinstein, D. Ritt, and E. E. Wilcox, "Tg-69: radiographic film for megavoltage beam dosimetry," *Medical physics*, vol. 34, no. 6Part1, pp. 2228–2258, 2007.

[59] A. Niroomand-Rad, C. R. Blackwell, B. M. Coursey, K. P. Gall, J. M. Galvin, W. L. McLaughlin, A. S. Meigooni, R. Nath, J. E. Rodgers, and C. G. Soares, "Radiochromic film dosimetry: recommendations of aapm radiation therapy committee task group 55," *Medical physics*, vol. 25, no. 11, pp. 2093–2115, 1998.

[60] M. A. Macchione, S. Lechón Páez, M. C. Strumia, M. Valente, and F. Mattea, "Chemical overview of gel dosimetry systems: A comprehensive review," *Gels*, vol. 8, no. 10, p. 663, 2022.

[61] M. Bero, W. Gilboy, and P. Glover, "Radiochromic gel dosemeter for three-dimensional dosimetry," *Radiation Physics and Chemistry*, vol. 61, no. 3-6, pp. 433–435, 2001.

[62] M. McJury, M. Oldham, V. Cosgrove, P. Murphy, S. Doran, M. Leach, and S. Webb, "Radiation dosimetry using polymer gels: methods and applications.," *The British Journal of Radiology*, vol. 73, no. 873, pp. 919–929, 2000.

[63] S. Awadalla, "Solid-state radiation detectors: technology and applications," 2017.

[64] I. G. DRAGANIĆ and Z. D. DRAGANIĆ, *The radiation chemistry of water*, vol. 26. Elsevier, 1971.

[65] J. W. Spinks and R. J. Woods, "An introduction to radiation chemistry," 1990.

[66] S. Le Caër, "Water radiolysis: influence of oxide surfaces on h_2 production under ionizing radiation," *Water*, vol. 3, no. 1, pp. 235–253, 2011.

[67] G. V. Buxton, C. L. Greenstock, W. P. Helman, and A. B. Ross, "Critical review of rate constants for reactions of hydrated electrons, hydrogen atoms and hydroxyl radicals ($^{\bullet}$oh/$^{\bullet}o^{-}$ in aqueous solution," *Journal of physical and chemical reference data*, vol. 17, no. 2, pp. 513–886, 1988.

[68] J. Keene, "Absorption spectra in irradiated water and some solutions. part ii. optical absorptions in irradiated water," *Nature*, vol. 197, 1963.

[69] F. Uhlig, O. Marsalek, and P. Jungwirth, "Unraveling the complex nature of the hydrated electron," *The Journal of Physical Chemistry Letters*, vol. 3, no. 20, pp. 3071–3075, 2012.

[70] D. C. Walker, "The hydrated electron," *Quarterly Reviews, Chemical Society*, vol. 21, no. 1, pp. 79–108, 1967.

[71] E. Hart and E. Fielden, "The hydrated electron dosimeter," 1970.

[72] M. Burton, "Radiation chemistry.," *The Journal of Physical Chemistry*, vol. 51, no. 2, pp. 611–625, 1947.

[73] J. H. Baxendale and F. Busi, *The Study of Fast Processes and Transient Species by Electron Pulse Radiolysis: Proceedings of the NATO Advanced Study Institute Held Ay Capri, Italy, 7–18 September, 1981*, vol. 86. Springer Science & Business Media, 2012.

[74] C. Ross, N. Klassen, and G. Smith, "The effect of various dissolved gases on the heat defect of water," *Medical physics*, vol. 11, no. 5, pp. 653–658, 1984.

[75] M. Klapper and M. Faraggi, "Applications of pulse radiolysis to protein chemistry," *Quarterly reviews of biophysics*, vol. 12, no. 4, pp. 465–519, 1979.

[76] S. Das, "Critical review of water radiolysis processes, dissociation products, and possible impacts on the local environment: a geochemist's perspective," *Australian Journal of Chemistry*, vol. 66, no. 5, pp. 522–529, 2013.

[77] H. Christensen and S. Sunder, "Current state of knowledge of water radiolysis effects on spent nuclear fuel corrosion," *Nuclear Technology*, vol. 131, no. 1, pp. 102–123, 2000.

[78] J. F. Sauvage, A. Flinders, A. J. Spivack, R. Pockalny, A. G. Dunlea, C. H. Anderson, D. C. Smith, R. W. Murray, and S. D'Hondt, "The contribution of water radiolysis to marine sedimentary life," *Nature communications*, vol. 12, no. 1, pp. 1–9, 2021.

[79] J. Baxendale, E. Fielden, and C. Capellos, "Pulse radiolysis," *Nature*, vol. 201, 1964.

[80] J. Ma, *Ultrafast Electron Transfer in Solutions Studied by Picosecond Pulse Radiolysis*. PhD thesis, Université Paris Saclay (COmUE), 2015.

[81] S. Gordon and E. J. Hart, "Spectrophotometric detection of hydrated electrons in co^{60} γ-ray irradiated solutions," *Journal of the American Chemical Society*, vol. 86, no. 23, pp. 5343–5344, 1964.

[82] V. Grigoryants, V. Lozovoy, Y. D. Chernousov, I. Shebolaev, V. Arutyunov, O. Anisimov, and Y. N. Molin, "Pulse radiolysis system with picosecond time resolution referred to cherenkov radiation," *Radiation physics and chemistry*, vol. 34, no. 3, pp. 349–352, 1989.

[83] T. Kozawa, Y. Mizutani, M. Miki, T. Yamamoto, S. Suemine, Y. Yoshida, and S. Tagawa, "Development of subpicosecond pulse radiolysis system," *Nuclear Instruments and Methods in Physics Research Section A: Accelerators, Spectrometers, Detectors and Associated Equipment*, vol. 440, no. 1, pp. 251–253, 2000.

[84] "Varian medical systems. truebeam stx system: Specifications.." report, 2015.

[85] E. Fielden and E. J. HART, "Hydrated electron and thermoluminescent dosimetry of pulsed x-ray beams," ACS Publications, 1968.

[86] "Thorlabs bb05-e02 dielectric mirror." Website. `https://www.thorlabs.com/thorproduct.cfm?partnumber=BB05-E02`.

[87] "Thorlabs det10a - si detector." Website. `https://www.thorlabs.com/thorproduct.cfm?partnumber=DET10A`.

[88] "Keysight. keysight infiniivision 2000 x-series oscilloscopes: Programmer's guide.." report, 2019.

[89] A. Bui, "Developing the hydrated electron dosimeter and investigation of the g-value of hydrated electrons," 2021.

[90] S. Incerti, G. Baldacchino, M. Bernal, R. Capra, C. Champion, Z. Francis, P. Gueye, A. Mantero, B. Mascialino, P. Moretto, *et al.*, "The geant4-dna project," *International Journal of Modeling, Simulation, and Scientific Computing*, vol. 1, no. 02, pp. 157–178, 2010.

[91] M. Dingfelder, D. Hantke, M. Inokuti, and H. G. Paretzke, "Electron inelastic-scattering cross sections in liquid water," *Radiation physics and chemistry*, vol. 53, no. 1, pp. 1–18, 1998.

[92] I. Plante and L. Devroye, "Considerations for the independent reaction times and step-by-step methods for radiation chemistry simulations," *Radiation Physics and Chemistry*, vol. 139, pp. 157–172, 2017.

[93] D. Boscolo, M. Krämer, M. Durante, M. Fuss, and E. Scifoni, "Trax-chem: A pre-chemical and chemical stage extension of the particle track structure code trax in water targets," *Chemical Physics Letters*, vol. 698, pp. 11–18, 2018.

[94] Y. Frongillo, T. Goulet, M. Fraser, V. Cobut, J. Patau, and J. Jay-Gerin, "Monte carlo simulation of fast electron and proton tracks in liquid water-ii. nonhomogeneous chemistry," *Radiation Physics and Chemistry*, vol. 51, no. 3, pp. 245–254, 1998.

[95] M. A. Bernal, M. C. Bordage, J. M. C. Brown, M. Davídková, E. Delage, Z. El Bitar, S. A. Enger, Z. Francis, S. Guatelli, V. N. Ivanchenko, *et al.*, "Track structure modeling in liquid water: A review of the geant4-dna very low energy extension of the geant4 monte carlo simulation toolkit," *Physica Medica*, vol. 31, no. 8, pp. 861–874, 2015.

[96] M. S. Kreipl, W. Friedland, and H. G. Paretzke, "Time-and space-resolved monte carlo study of water radiolysis for photon, electron and ion irradiation," *Radiation and environmental biophysics*, vol. 48, no. 1, pp. 11–20, 2009.

[97] J. Ramos-Méndez, W.-g. Shin, M. Karamitros, J. Domínguez-Kondo, N. H. Tran, S. Incerti, C. Villagrasa, Y. Perrot, V. Štěpán, S. Okada, *et al.*, "Independent reaction times method in geant4-dna: Implementation and performance," *Medical physics*, vol. 47, no. 11, pp. 5919–5930, 2020.

[98] D. M. Bartels, A. R. Cook, M. Mudaliar, and C. D. Jonah, "Spur decay of the solvated electron in picosecond radiolysis measured with time-correlated absorption

spectroscopy," *The Journal of Physical Chemistry A*, vol. 104, no. 8, pp. 1686–1691, 2000.

[99] A. K. El Omar, U. Schmidhammer, P. Jeunesse, J.-P. Larbre, M. Lin, Y. Muroya, Y. Katsumura, P. Pernot, and M. Mostafavi, "Time-dependent radiolytic yield of oh• radical studied by picosecond pulse radiolysis," *The Journal of Physical Chemistry A*, vol. 115, no. 44, pp. 12212–12216, 2011.

[100] F. Wang, U. Schmidhammer, J.-P. Larbre, Z. Zong, J.-L. Marignier, and M. Mostafavi, "Time-dependent yield of the hydrated electron and the hydroxyl radical in d_2o: A picosecond pulse radiolysis study," *Physical Chemistry Chemical Physics*, vol. 20, no. 23, pp. 15671–15679, 2018.

[101] H. Yoshida, W. E. Bolch, K. B. Jacobson, and J. E. Turner, "Measurement of free ammonia produced by x irradiation of glycylglycine in aqueous solution," *Radiation research*, vol. 121, no. 3, pp. 257–261, 1990.

[102] S. Incerti, A. Ivanchenko, M. Karamitros, A. Mantero, P. Moretto, H. Tran, B. Mascialino, C. Champion, V. Ivanchenko, M. Bernal, *et al.*, "Comparison of geant4 very low energy cross section models with experimental data in water," *Medical physics*, vol. 37, no. 9, pp. 4692–4708, 2010.

[103] M. Karamitros, S. Luan, M. A. Bernal, J. Allison, G. Baldacchino, M. Davidkova, Z. Francis, W. Friedland, V. Ivantchenko, A. Ivantchenko, *et al.*, "Diffusion-controlled

reactions modeling in geant4-dna," *Journal of Computational Physics*, vol. 274, pp. 841–882, 2014.

[104] V. Michalik, M. Begusova, and E. Bigildeev, "Computer-aided stochastic modeling of the radiolysis of liquid water," *Radiation research*, vol. 149, no. 3, pp. 224–236, 1998.

[105] M. H. Peters, "The smoluchowski diffusion equation for structured macromolecules near structured surfaces," *The Journal of Chemical Physics*, vol. 112, no. 12, pp. 5488–5498, 2000.

[106] B. P. Ölveczky and A. Verkman, "Monte carlo analysis of obstructed diffusion in three dimensions: application to molecular diffusion in organelles," *Biophysical journal*, vol. 74, no. 5, pp. 2722–2730, 1998.

[107] I. Plante, "A monte-carlo step-by-step simulation code of the non-homogeneous chemistry of the radiolysis of water and aqueous solutions—part ii: calculation of radiolytic yields under different conditions of let, ph, and temperature," *Radiation and environmental biophysics*, vol. 50, no. 3, pp. 405–415, 2011.

[108] V. Cobut, Y. Frongillo, J. Patau, T. Goulet, M. Fraser, and J. Jay-Gerin, "Monte carlo simulation of fast electron and proton tracks in liquid water-i. physical and physicochemical aspects," *Radiation Physics and Chemistry*, vol. 51, no. 3, pp. 229–244, 1998.

[109] J. Meesungnoen and J.-P. Jay-Gerin, "High-let radiolysis of liquid water with $^{1}h^{+}$, $^{4}he^{2+}$, $^{1}2c^{6+}$, and $^{2}0ne^{9+}$ ions: effects of multiple ionization," *The Journal of Physical Chemistry A*, vol. 109, no. 29, pp. 6406–6419, 2005.

[110] M. Hill and F. Smith, "Calculation of initial and primary yields in the radiolysis of water," *Radiation physics and chemistry*, vol. 43, no. 3, pp. 265–280, 1994.

[111] N. Green, M. Pilling, S. Pimblott, and P. Clifford, "Stochastic modeling of fast kinetics in a radiation track," *Journal of Physical Chemistry*, vol. 94, no. 1, pp. 251–258, 1990.

[112] M. Terrissol and A. Beaudre, "Simulation of space and time evolution of radiolytic species induced by electrons in water," *Radiation Protection Dosimetry*, vol. 31, no. 1-4, pp. 175–177, 1990.

[113] P. Clifford, N. J. Green, and M. J. Pilling, "Stochastic model based on pair distribution functions for reaction in a radiation-induced spur containing one type of radical," *The Journal of Physical Chemistry*, vol. 86, no. 8, pp. 1318–1321, 1982.

[114] P. Clifford, N. J. Green, and M. J. Pilling, "Monte carlo simulation of diffusion and reaction in radiation-induced spurs. comparisons with analytic models," *The Journal of Physical Chemistry*, vol. 86, no. 8, pp. 1322–1327, 1982.

[115] P. Clifford, N. J. Green, M. J. Oldfield, M. J. Pilling, and S. M. Pimblott, "Stochastic models of multi-species kinetics in radiation-induced spurs," *Journal of the Chemical*

Society, Faraday Transactions 1: Physical Chemistry in Condensed Phases, vol. 82, no. 9, pp. 2673–2689, 1986.

[116] T. Goulet, M.-J. Fraser, Y. Frongillo, and J.-P. Jay-Gerin, "On the validity of the independent reaction times approximation for the description of the nonhomogeneous kinetics of liquid water radiolysis," *Radiation Physics and Chemistry*, vol. 51, no. 1, pp. 85–91, 1998.

[117] A. Bui, H. Bekerat, L. Childress, J. Sankey, J. Seuntjens, and S. A. Enger, "Effects of incoming particle energy and cluster size on the g-value of hydrated electrons," *Physica Medica*, vol. 107, p. 102540, 2023.

[118] "Chapter seven - radiation sources and irradiation techniques," in *The Radiation Chemistry of Water* (I. G. DRAGANIĆ and Z. D. DRAGANIĆ, eds.), vol. 26 of *Physical Chemistry*, pp. 191–210, Elsevier, 1971.

[119] K. Sehested, H. Corfitzen, and H. Fricke, "Cobalt-60 γ-ray radiolysis of aqueous solutions of $h_2 + o_2$. determination of $g_{e^-_{aq}} + g_h$ at ph 0.46-6.5," *The Journal of Physical Chemistry*, vol. 74, no. 1, pp. 211–213, 1970.

[120] K. Sehested, E. Bjergbakke, and H. Fricke, "The primary species yields in the ^{60}co γ-ray radiolysis of aqueous solutions of h_2so_4 between ph 7 and 0.46," *Radiation Research*, vol. 56, no. 2, pp. 385–399, 1973.

[121] S. Sanguanmith, J. Meesungnoen, and J.-P. Jay-Gerin, "Time-dependent yield of oh radicals in the low linear energy transfer radiolysis of water between 25 and 350°c," *Chemical Physics Letters*, vol. 588, pp. 82–86, 2013.

[122] A. Sultana, J. Meesungnoen, and J.-P. Jay-Gerin, "Yields of primary species in the low-linear energy transfer radiolysis of water in the temperature range of 25–700°c," *Physical Chemistry Chemical Physics*, vol. 22, no. 14, pp. 7430–7439, 2020.

[123] A. Catenaccio, Y. Daruich, and C. Magallanes, "Temperature dependence of the permittivity of water," *Chemical physics letters*, vol. 367, no. 5-6, pp. 669–671, 2003.

[124] M. Lin, Y. Katsumura, Y. Muroya, H. He, G. Wu, Z. Han, T. Miyazaki, and H. Kudo, "Pulse radiolysis study on the estimation of radiolytic yields of water decomposition products in high-temperature and supercritical water: use of methyl viologen as a scavenger," *The Journal of Physical Chemistry A*, vol. 108, no. 40, pp. 8287–8295, 2004.

[125] H. Shiraishi, G. V. Buxton, and N. D. Wood, "Temperature dependence of the absorption spectrum of the methyl viologen cation radical and use of methyl viologen as a scavenger for estimating yields of the primary radicals in the radiolysis of high-temperature water," *International Journal of Radiation Applications and Instrumentation. Part C. Radiation Physics and Chemistry*, vol. 33, no. 6, pp. 519–522, 1989.

[126] N. Autsavapromporn, J. Meesungnoen, I. Plante, and J.-P. Jay-Gerin, "Monte carlo simulation study of the effects of acidity and let on the primary free-radical and molecular yields of water radiolysis-application to the fricke dosimeter," *Canadian journal of chemistry*, vol. 85, no. 3, pp. 214–229, 2007.

[127] H. Schuessler and R. Sieber, "Radiolysis of dna studied by hpl-gel chromatography," *International journal of radiation biology*, vol. 63, no. 4, pp. 437–444, 1993.

[128] V. Štepán and M. Davídková, "Impact of oxygen concentration on yields of dna damages caused by ionizing radiation," in *Journal of Physics: Conference Series*, vol. 101, p. 012015, IOP Publishing, 2008.

[129] J. F. Ward, "Dna damage produced by ionizing radiation in mammalian cells: identities, mechanisms of formation, and reparability," *Progress in nucleic acid research and molecular biology*, vol. 35, pp. 95–125, 1988.

[130] I. Al-Nabulsi and K. T. Wheeler, "Radiation-induced dna damage in tumors and normal tissues: V. influence of ph and nutrient depletion on the formation of dna-protein crosslinks in irradiated partially and fully hypoxic tumor cells," *Radiation research*, vol. 151, no. 2, pp. 188–194, 1999.

[131] M.-A. Hervé du Penhoat, T. Goulet, Y. Frongillo, M.-J. Fraser, P. Bernat, and J.-P. Jay-Gerin, "Radiolysis of liquid water at temperatures up to 300°c: A monte carlo

simulation study," *The Journal of Physical Chemistry A*, vol. 104, no. 50, pp. 11757–11770, 2000.

[132] V. Favaudon, L. Caplier, V. Monceau, F. Pouzoulet, M. Sayarath, C. Fouillade, M.-F. Poupon, I. Brito, P. Hupé, J. Bourhis, *et al.*, "Ultrahigh dose-rate flash irradiation increases the differential response between normal and tumor tissue in mice," *Science translational medicine*, vol. 6, no. 245, pp. 245ra93–245ra93, 2014.

[133] E. S. Diffenderfer, I. I. Verginadis, M. M. Kim, K. Shoniyozov, A. Velalopoulou, D. Goia, M. Putt, S. Hagan, S. Avery, K. Teo, *et al.*, "Design, implementation, and in vivo validation of a novel proton flash radiation therapy system," *International Journal of Radiation Oncology* Biology* Physics*, vol. 106, no. 2, pp. 440–448, 2020.

Appendix A

Reaction Rate Constants

Based on the reaction rate constants, the diffusion-controlled reactions may be classified into six types (2; 94). Type 1 reactions are totally diffusion controlled (Table A1), which means that their reaction rates are completely governed by diffusion. Type 2 reactions are partially diffusion controlled (Tables A2, A3, A4, A5), their reaction rates are governed by diffusion but also the reaction rates of reactive loss (loss of reactants). Type 3 reactions are totally diffusion controlled, but their reactants are both ions, so electrical interactions must be considered (Table A6). Type 4 reactions are partially diffusion controlled, but their reactants are also ions (Table A7). Type 5 reactions are totally diffusion controlled, but the molecular spin is considered in the equation. Finally, type 6 reactions are non-diffusion controlled and are mainly first-order or pseudo-first-order reactions (Table A8). Pseudo-first order reactions are those where one of the reactants has a considerably higher concentration

than the other reactants and is considered to be a "background molecule" (92; 107).

Type 1 Reactions		
Reaction	Polynomial ($M^{-1}s^{-1}$)	Value at 298.15 k (25°C)
R1.1: $H + H \longrightarrow H_2$	$2.70\times\ 10^{12}e^{(-1867.5/t)}$	0.51×10^{10}
R1.2: $e^-_{aq} + H + (H_2O) \longrightarrow H_2 + OH^-$	$1.14\times10^{13}e^{-1795.7/t}$	2.76×10^{10}
R1.3: $H + O(3\,p) \longrightarrow OH$	$2.03\times10^{10}\ e^{-12.6/(Rt)\ddagger}$	2.02×10^{10}
R1.4: $H + O^- \longrightarrow OH^-$	$2.03\times10^{10}e^{-12.6/(Rt)\ddagger}$	2.02×10^{10}
R1.5: $OH + O(3\,p) \longrightarrow HO_2$	$2.03\times10^{10}e^{-12.6/(Rt)\ddagger}$	2.02×10^{10}
R1.6: $HO_2 + O(3\,p) \longrightarrow O_2 + OH$	$2.03\times10^{10}e^{-12.6/(Rt)\ddagger}$	2.02×10^{10}
R1.7: $O(3\,p) + O(3\,p) \longrightarrow O_2$	$2.21\times10^{10}e^{-12.6/(Rt)\ddagger}$	2.20×10^{10}

Table A1: Temperature-dependent polynomials of reaction rate constants of type 1 (totally diffusion controlled) reactions with the gas constant (R) taken as 8.31 $J{\cdot}K^{-1}$ and temperature t in Kelvin. Values at 25°C are also indicated. When not specified, polynomial values are from (1). Otherwise, the references are: (†)(2), (‡)(3).

Type 2 Reactions		
Reaction	Polynomial ($M^{-1}s^{-1}$)	Value at 298.15 k (25°C)
R2.1: $OH + H \longrightarrow H_2O$	$4.26\times10^{11}e^{-1091.9/t}$	$1.09\times\ 10^{10}$
R2.2: $H + H_2O_2 \longrightarrow OH + H_2O$	$1.79\times10^{11}e^{-2533.6/t}$	3.65×10^{7}
R2.3: $H + OH^- \rightleftharpoons e^-_{aq} + H_2O$	$\log R2.3 = 22.970 - 1.971\times10^4/t + 1.137\times10^7/t^2 - 2.991\times10^9/t^3 + 2.803\times10^{11}/t^4$	2.44×10^{7}
R2.4: $H + O_2 \longrightarrow HO_2$	$\mathrm{Log}R2.4 = 10.704 + 2.840\times10^2/t - 1.369\times10^5/t^2$	1.31×10^{10}
R2.5: $H + HO_2 \longrightarrow H_2O_2$	$5.17\times10^{12}e^{-1824.2/t}$	1.13×10^{10}
R2.6: $H + O_2^- \longrightarrow HO_2^-$	$5.17\times10^{12}e^{-1824.2/t}$	1.13×10^{10}
R2.7: $OH + OH \longrightarrow H_2O_2$	$\mathrm{Log}R2.7 = 8.054 + 2.193\times10^3/t - 7.395\times10^5/t^2 + 6.870\times10^7/t^3$	4.81×10^{9}
R2.8:$OH + H_2O_2 \longrightarrow HO_2 + H_2O$	$7.68\times10^{9}e^{-1661.4/t}$	2.90×10^{7}

Table A2: Temperature-dependent polynomials of reaction rate constants of type 2 (1/4) (partially diffusion controlled) reactions with the gas constant (R) taken as 8.31 J·K^{-1} and temperature t in Kelvin. Values at 25°C are also indicated. When not specified, polynomial values are from (1). Otherwise, the references are: (†)(2), (‡)(3).

Type 2 Reactions		
Reaction	Polynomial ($M^{-1}s^{-1}$)	Value at 298.15 k (25°C)
R2.9: $OH + H_2 \longrightarrow H + H_2O$	$\mathrm{Log}R2.9 = -11.556 + 3.2546\times10^4/t - 1.8623\times10^7/t^2 + 4.5543\times10^9/t^3 - 4.1364\times10^{11}/t^4$	3.95×10^{7}
R2.10: $e^-_{aq} + OH \longrightarrow OH^-$	$\mathrm{Log}R2.10 = 13.123 - 1.023\times10^3/t + 7.634\times10^4/t^2$	3.55×10^{10}
R2.11: $OH + OH^- \longrightarrow O^- + H_2O$	$\mathrm{Log}R2.11 = 13.339 - 2.220\times10^3/t + 7.333\times10^5/t^2 - 1.065\times10^8/t^3$	1.33×10^{10}
R2.12: $OH + HO_2 \longrightarrow O_2 + H_2O$	$1.29\times10^{11}e^{-799.2/t}$	8.84×10^{9}
R2.13: $OH + O_2^- \longrightarrow O_2 + OH^-$	$8.77\times10^{11}e^{-1306.2/t}$	1.09×10^{10}
R2.14: $OH + HO_2^- \longrightarrow H_2O + O_2^-$	$4.5\times10^{12}e^{-1877.71360/t}$†	8.29×10^{9}
R2.15: $HO_2^- + O^- \longrightarrow OH^- + O_2^-$	$1.45\times10^{13}e^{-2928.5/t}$	7.86×10^{8}
R2.16: $OH + O_3^- \longrightarrow O_2^- + HO_2$	$8.77\times10^{11}e^{-1306.2/t}$	1.09×10^{10}

Table A3: Temperature-dependent polynomials of reaction rate constants of type 2 (2/4) (partially diffusion controlled) reactions with the gas constant (R) taken as 8.31 J·K^{-1} and temperature t in Kelvin. Values at 25°C are also indicated. When not specified, polynomial values are from (1). Otherwise, the references are: (†)(2), (‡)(3).

Type 2 Reactions		
Reaction	Polynomial ($M^{-1}s^{-1}$)	Value at 298.15 k (25°C)
R2.17: $e^-_{aq} + H_2O_2 \longrightarrow OH^- + OH$	$7.70\times10^{12}e^{-1889.6/t}$	1.36×10^{10}
R2.18: $H_2O_2 + OH^- \rightleftharpoons HO_2^- + H_2O$	LogR2.18 = 13.339 - $2.220\times10^3/t$ + $7.333\times10^5/t^2$ - $1.065\times10^8/t^3$	1.33×10^{10}
R2.19: $H_2O_2 + O(3\,p) \longrightarrow HO_2 + OH$	$2.99\times10^{11}e^{-1876.36438/t}$†	5.53×10^8
R2.20: $H_2O_2 + O^- \longrightarrow HO_2 + OH^-$	$2.99\times10^{11}e^{-1876.36438/t}$†	5.53×10^8
R2.21: $H_2 + O(3\,p) \longrightarrow OH + H$	$4.837\times10^3e^{-34.9/(Rt)}$‡	4.77×10^3
R2.22: $H_2 + O^- \longrightarrow H + OH^-$	$2.32\times10^{10}e^{-1550.5/t}$	1.28×10^8
R2.23: $e^-_{aq} + O_2 \longrightarrow O_2^-$	$2.52\times10^{12}e^{-1401.5/t}$	2.29×10^{10}
R2.24: $e^-_{aq} + HO_2 \longrightarrow HO_2^-$	$2.46\times10^{12}e^{-1563.6/t}$	1.30×10^{10}

Table A4: Temperature-dependent polynomials of reaction rate constants of type 2 (3/4) (partially diffusion controlled) reactions with the gas constant (R) taken as 8.31 J·K^{-1} and temperature t in Kelvin. Values at 25°C are also indicated. When not specified, polynomial values are from (1). Otherwise, the references are: (†)(2), (‡)(3).

Type 2 Reactions		
Reaction	Polynomial ($M^{-1}s^{-1}$)	Value at 298.15 k (25°C)
R2.25: $OH^- + HO_2 \rightleftharpoons O_2^- + H_2O$	LogR2.25 = 13.339 - $2.220\times10^3/t$ + $7.333\times10^5/t^2$ - $1.065\times10^8/t^3$	1.33×10^{10}
R2.26: $OH^- + O(3\,p) \longrightarrow HO_2^-$	$1.45\times10^{13}e^{-2928.5/t}$	7.86×10^8
R2.27: $O_2 + O(3\,p) \longrightarrow O_3$	$3.41\times10^{11}e^{-1344.9/t}$	3.74×10^9
R2.28: $O_2 + O^- \rightleftharpoons O_3^-$	$3.41\times10^{11}e^{-1344.9/t}$	3.74×10^9
R2.29: $HO_2 + HO_2 \longrightarrow H_2O_2 + O_2$	$2.78\times10^9e^{-2416.4/t}$	8.40×10^5
R2.30: $HO_2 + O_2^- + H_2O \longrightarrow H_2O_2 + O_2 + OH^-$	$2.63\times10^9e^{-974.3/t}$	1.00×10^8
R2.31: $HO_2 + O(3\,p) \longrightarrow O_2 + OH$	$2.03\times10^{10}e^{-12.6/(Rt)}$‡	2.02×10^{10}

Table A5: Temperature-dependent polynomials of reaction rate constants of type 2 (4/4) (partially diffusion controlled) reactions with the gas constant (R) taken as 8.31 J·K^{-1} and temperature t in Kelvin. Values at 25°C are also indicated. When not specified, polynomial values are from (1). Otherwise, the references are: (†)(2), (‡)(3).

Type 3 Reactions		
Reaction	Polynomial ($M^{-1}s^{-1}$)	Value at 298.15 k (25°C)
R3.1: $e^-_{aq} + e^-_{aq} + 2\,H_2O \longrightarrow H_2 + 2\,OH^-$	LogR3.1 = 12.281 - $3.786\times10^2/t$ - $6.673\times10^4/t^2$ - $1.075\times10^7/t^3$	7.16×10^9
R3.2: $H_3O^+ + OH^- \rightleftharpoons 2\,H_2O$	LogR3.2 = 20.934 - $1.236\times10^4/t$ + $6.364\times10^6/t^2$ - $1.475\times10^9/t^3$ + $1.237\times10^11/t^4$	1.18×10^{11}
R3.3: $H_3O^+ + O_2^- \longrightarrow H_2O + HO_2$	LogR3.3 = 16.410 - $4.888\times10^3/t$ + $1.622\times10^6/t^2$ - $2.004\times10^8/t^3$	5.02×10^{10}

Table A6: Temperature-dependent polynomials of reaction rate constants of type 3 (totally diffusion controlled with reactants of ions) reactions with the gas constant (R) taken as 8.31 $J{\cdot}K^{-1}$ and temperature t in Kelvin. Values at 25°C are also indicated. When not specified, polynomial values are from (1). Otherwise, the references are: (†)(2), (‡)(3).

Type 4 Reactions		
Reaction	Polynomial ($M^{-1}s^{-1}$)	Value at 298.15 k (25°C)
R4.1: $e^-_{aq} + H_3O^+ \rightleftharpoons H + H_2O$	LogR4.1 = 39.127 - $3.888\times10^4/t$ + $2.054\times10^7/t^2$- $4.899\times10^9/t^3$+ $4.376\times10^{11}/t^4$	2.10×10^{10}
R4.2: $e^-_{aq} + O_2^- + H_2O \longrightarrow H_2O_2 + 2\,OH^-$	$2.46\times10^{12}e^{-1563.6/t}$	1.30×10^{10}
R4.3: $e^-_{aq} + HO_2^- \longrightarrow O^- + OH^-$	$1.75\times10^{12}e^{-1852.77/t}$†	3.50×10^9
R4.4: $e^-_{aq} + O^- \longrightarrow OH^- + OH^-$	$5.6\times10^{11}e^{-951.64/t}$†	2.31×10^{10}
R4.5: $H_3O^+ + O_2^- \longrightarrow HO_2 + H_2O$	LogR4.5 = 16.410 - $4.888\times10^3/t$ + $1.622\times10^6/t^2$ -$2.004\times10^8/t^3$	5.02×10^{10}
R4.6: $H_3O^+ + HO_2^- \longrightarrow H_2O_2 + H_2O$	LogR4.6 = 16.410 - $4.888\times10^3/t$ + $1.622\times10^6/t^2$ -$2.004\times10^8/t^3$	5.02×10^{10}
R4.7: $H_3O^+ + O^- \longrightarrow OH + H_2O$	LogR4.7 = 16.410 - $4.888\times10^3/t$ + $1.622\times10^6/t^2$ -$2.004\times10^8/t^3$	5.02×10^{10}
R4.8: $O_2^- + O^- + H_2O \longrightarrow O_2^- + OH^- + OH^-$	$3.41\times10^{11}e^{-1344.9/t}$	3.74×10^9
R4.9: $HO_2^- + O^- \longrightarrow O_2^- + OH^-$	$1.45\times10^{13}e^{-2928.5/t}$	7.86×10^8
R4.10: $O^- + O^- + 2\,H_2O \longrightarrow H_2O_2 + OH^- + OH^-$	2.21×10^{10} $e^{-12.6/(Rt)}$‡	2.20×10^{10}
R4.11: $O^- + O_3^- \longrightarrow O_2^- + O_2^-$	$3.41\times10^{11}e^{-1344.9/t}$‡	3.74×10^9

Table A7: Temperature-dependent polynomials of reaction rate constants of type 4 (partially diffusion controlled with reactants of ions) reactions with the gas constant (R) taken as 8.31 J·K^{-1} and temperature t in Kelvin. Values at 25°C are also indicated. When not specified, polynomial values are from (1). Otherwise, the references are: (†)(2), (‡)(3).

Type 6 Reactions		
Reaction	Polynomial (s^{-1})	Value at 298.15 k (25°C)
R6.1: $O_3^- + O^- \longrightarrow 2\,O_2^-$	$3.20\times10^{11}e^{-5552.1/t}$	2.6×10^3
R6.2: $HO_2 + H_2O \longrightarrow H_3^+ + O_2^-$	R4.5·K_{HO_2} · $[H_2O]$	4.28×10^7
R6.3: $H + H_2O \longrightarrow e_{aq}^- + H_3O^+$	R4.1·K_H · $[H_2O]$	3.23×10^2
R6.4: $e_{aq}^- + H_2O \longrightarrow H + OH^-$	$\frac{R2.3\cdot K_{H_2O}}{K_H}$ · $[H_2O]$	8.73×10^2
R6.5: $O_2^- + H_2O \longrightarrow HO_2 + OH^-$	$2.266\times10^{10}e^{-2897.95134/t}\cdot[H_2O]$†	7.54×10^7
R6.6: $HO_2^- + H_2O \longrightarrow H_2O_2 + OH^-$	$\frac{R2.18\cdot K_{H_2O}}{K_{H_2O_2}}$ · $[H_2O]$	7.05×10^7
R6.7: $O(3\,p) + H_2O \longrightarrow OH + OH$	$18.4048\times10^{-41.4/(Rt)}$‡	1.00×10^3
R6.8: $O^- + H_2O \longrightarrow OH + OH^-$	$\frac{R2.18\cdot K_{H_2O}}{K_{H_2O_2}}$ · $[H_2O]$	7.05×10^7
R6.9: $e_{aq}^- + H_3O^+(B) \longrightarrow H + H_2O$	R4.1·$[H_3O^+(B)]$	2.07×10^3
R6.10: $O_2^- + H_3O^+(B) \longrightarrow HO_2 + H_2O$	R4.5·$[H_3O^+(B)]$	4.97×10^3
R6.11: $OH^- + H_3O^+(B) \longrightarrow 2\,H_2O$	R3.2·$[H_3O^+(B)]$	1.16×10^4
R6.12: $H_3O^+ + OH^-(B) \longrightarrow 2\,H_2O$	R3.2·$[OH^-(B)]$	1.16×10^4
R6.13: $HO_2^- + H_3O^+(B) \longrightarrow H_2O_2 + H_2O$	R4.6·$[H_3O^+(B)]$	4.97×10^3
R6.14: $O^- + H_3O^+(B) \longrightarrow OH + H_2O$	R4.7·$[H_3O^+(B)]$	4.97×10^3
R6.15: $O_3^- + H_3O^+(B) \longrightarrow OH + O_2 + H_2O$	R3.3·$[H_3O^+(B)]$	4.97×10^3
R6.16: $H + OH^-(B) \longrightarrow H_2O + e_{aq}^-$	R2.3·$[OH^-(B)]$	2.41
R6.17: $OH + OH^-(B) \longrightarrow O^- + H_2O$	R2.11·$[OH^-(B)]$	1.32×10^3
R6.18: $H_2O_2 + OH^-(B) \longrightarrow HO_2^- + H_2O$	R2.18·$[OH^-(B)]$	1.32×10^3
R6.19: $HO_2 + OH^-(B) \longrightarrow O_2^- + H_2O$	R2.25 · $[OH^-(B)]$	1.32×10^3
R6.20: $O + OH^-(B) \longrightarrow HO_2^-$	R2.26 · $[OH^-(B)]$	7.78×10^1

Table A8: Temperature-dependent polynomials of reaction rate constants of type 6 (non-diffusion controlled) reactions with the gas constant (R) taken as 8.31 $J{\cdot}K^{-1}$ and temperature t in Kelvin. Values at 25°C are also indicated. When not specified, polynomial values are from (1). The K values, expressed in Molar units, are taken from (1). Otherwise, the references are: (†)(2), (‡)(3). (B) means the background species.

Appendix B

Diffusion Coefficients

Diffusion Coefficient	
D	Polynomial (m^2s^{-1})
D_{OH}	$(0.00408 \cdot t^{1.38897}$ + p·(1.0/t² -174613.7394/t + 847.03131 - 0.71041t) + p²·log(p)·(1.0/t² - 15364.1999/t + 782.41564- 0.64852t) + p²·(1.0/t² + 163191.6423/t - 795.71944 + 0.634849t)$1e^{-9}$
D_{O_2}	$1.82779 \cdot t^{0.422868}$ + p·(1.0/t² - 102443/t + 334.021- 0.119239t) + p²·log(p)·(1.0/t² - 102959/t + 334.195 - 0.117517t)+ p²·(1.0/t² + 100433/t - 347.059 + 0.125558t)·$1e^{-9}$
D_{H_2}	$116.211 \cdot t^{0.0538917}$ + p·(1.0/t² +372312/t - 1794.21 + 1.42193t) + p²·1log(p)·(1.0/t² + 476427/t - 1880.99+ 1.6233·t) + p²·(1.0/t² - 377905/t + 1654.15- 1.39764t)·$1e^{-9}$
$D_{O_2^-}$	$1.82779 \cdot t^{0.42268}$ + p·(1.0/t² -102443/t +334.021 -0.119239t)+ p²·log(p)·(1.0/t² - 102959/t + 334.195 - 0.117517·t) + p²·(1.0/t²+ 100433/t - 347.059 + 0.125558·t) - 0.55152409 - 0.25)·$1e^{-9}$ = D_{O_2}scaled
$D_{O_3^-}$	$((1.82779 \cdot t^{0.42268}$ + p·(1.0/t² -102443/t +334.021 -0.119239t)+ p²·log(p)·(1.0/t² - 102959/t + 334.195 - 0.117517t) + p²·(1.0/t²+ 100433/t - 347.059 + 0.125558t) - 0.55152409)·$1e^{-9}$ = D_{O_2}scaled
D_{O_3}	$D_{O_3} = D_{O_3^-}$
$D_{O(3p)}$	$D_{O(3p)} = D_{O_3^-}$
D_{O^-}	$D_{O^-} = D_{O_3^-}$

Table B1: Diffusion coefficients (1/2) in units of m^2s^{-1} with ρ = density, t in Kelvin and T in Celsius. When not specified, polynomials are from (4). Otherwise, the references are: (†)(2), (⋆)(5).

Diffusion Coefficient	
D	Polynomial (m^2s^{-1})
D_H^+†	$5.361\times10^{-9}+1.659\times10^{-10}T-7.48\times10^{-14}T^2 - 1.0018\times10^{-16}T^3$
$D_{H_2O_2}$†	$(0.0046471\cdot t^{1.2939}+p\cdot(1.05646\times10^8/t^2-511648/t+ 691.903 - 0.1729t) +$ $p^2\cdot\log(p)\cdot(8.88978\times10^7/t^2 - 358381/t + 334.773 + 0.0213276t)+$ $p^2\cdot(-1.01281\times10^8/t^2 + 475755/t - 608.627 +0.116203t))\cdot1e^{-9}$
D_{OH^-}†	$2.666\times10^{-9}+ 9.769\times10^{-11}T +3.303\times10^{-13}T^2- 7.295\times10^{-16}T^3$
D_H†	$5.361\times10^{-9}+1.659\times10^{-10}T-7.48\times10^{-14}T^2- 1.0018\times10^{-16}T^3$ $- 2.46\times10^{-09} = D_{H^+}$ scaled
D_{HO_2}†	$D_{HO_2} = D_{H_2O_2}$
$D_{HO_2^-}$†	$(0.0046471\cdot t^{1.2939}+p\cdot(1.05646\times10^8/t^2-511648/t+ 691.903 - 0.1729t)+$ $p^2\cdot\log(p)\cdot(8.88978\times10^7/t^2 - 358381/t + 334.773 + 0.0213276t)+p^2\cdot(-1.01281\times10^8/t^2 +$ $475755/t - 608.627 +0.116203t)-1.034362355)\cdot1e^{-9}$
$D_{e^-_{aq}}$ ⋆	$10^{-0.7638-1058.18/T(254.92/T)^{40}}e^{-4}$

Table B2: Diffusion coefficients (2/2) in units of m^2s^{-1} with ρ = density, t in Kelvin and T in Celsius. When not specified, polynomials are from (4). Otherwise, the references are: (†)(2), (⋆)(5).

Appendix C

Water Properties

Water Properties	
Water property	Polynomial
$[H_2O]$(mole/L)	$55.50 + 6.075\times10^{-3}$t-$4.110\times10^{-4}t^2 + 1.496\times10^{-6}t^3-2.619\times10^{-9}$t^4

Table C1: Water property from (1) with temperature t in Celsius.